

Gauging the effect of Supermassive Black Holes feedback on Quasar host galaxies

B. Dall’Agnol de Oliveira^{1*}, T. Storchi-Bergmann^{1,2}, S. B. Kraemer³,
M. Villar Martín⁴, A. Schnorr-Müller¹, H. R. Schmitt⁵, D. Ruschel-Dutra⁶,
D. M. Crenshaw⁷, T. C. Fischer⁸

¹*Departamento de Astronomia, Universidade Federal do Rio Grande do Sul, IF, CP 15051, 91501-970 Porto Alegre, RS, Brazil*

²*Harvard-Smithsonian Center for Astrophysics, 60 Garden St., Cambridge, MA 02138, USA*

³*Institute for Astrophysics and Computational Sciences, Department of Physics, The Catholic University of America, Washington, DC 20064, USA*

⁴*Centro de Astrobiología (INTA-CSIC), Ctra. de Torrejón a Ajalvir, km 4, 28850 Torrejón de Ardoz, Madrid, Spain*

⁵*Naval Research Laboratory, Washington, DC 20375, USA*

⁶*Departamento de Física, Universidade Federal de Santa Catarina, P.O. Box 476, 88040-900, Florianópolis, SC, Brazil*

⁷*Department of Physics and Astronomy, Georgia State University, Astronomy Offices, 25 Park Place, Suite 600, Atlanta, GA 30303, US*

⁸*AURA for ESA, Space Telescope Science Institute, 3700 San Martin Drive, Baltimore, MD 21218*

Accepted: 13 April 2021

ABSTRACT

In order to gauge the role that active galactic nuclei (AGN) play in the evolution of galaxies via the effect of kinetic feedback in nearby QSO 2’s ($z \sim 0.3$), we observed eight such objects with bolometric luminosities $L_{bol} \sim 10^{46} \text{erg s}^{-1}$ using Gemini GMOS-IFU’s. The emission lines were fitted with at least two Gaussian curves, the broadest of which we attributed to gas kinetically disturbed by an outflow. We found that the maximum extent of the outflow ranges from ~ 1 to 8 kpc, being $\sim 0.5 \pm 0.3$ times the extent of the [O III] ionized gas region. Our ‘default’ assumptions for the gas density (obtained from the [S II] doublet) and outflow velocities resulted in peak mass outflow rates of $\dot{M}_{out}^{def} \sim 3 - 30 M_{\odot} \text{yr}^{-1}$ and outflow power of $\dot{E}_{out}^{def} \sim 10^{41} - 10^{43} \text{erg s}^{-1}$. The corresponding kinetic coupling efficiencies are $\epsilon_f^{def} = \dot{E}_{out}^{def} / L_{bol} \sim 7 \times 10^{-4} - 0.5\%$, with the average efficiency being only 0.06% (0.01% median), implying little feedback powers from ionized gas outflows in the host galaxies. We investigated the effects of varying assumptions and calculations on \dot{M}_{out} and \dot{E}_{out} regarding the ionized gas densities, velocities, masses and inclinations of the outflow relative to the plane of the sky, resulting in average uncertainties of one dex. In particular, we found that better indicators of the [O III] emitting gas density than the default [S II] line ratio, such as the [Ar IV] $\lambda\lambda 4711, 40$ line ratio, result in almost an order of magnitude decrease in the ϵ_f .

Key words: galaxies: active – quasars: emission lines – ISM: jets and outflows – quasars: supermassive black holes

1 INTRODUCTION

In Active Galactic Nuclei (AGN), the mass accretion to a nuclear supermassive black hole (SMBH) leads to emission of radiation, accretion disk winds and jets from its vicinity – the so-called AGN feedback processes (Fabian 2012; Heck-

man & Best 2014; Harrison et al. 2018). In galaxy evolution models (e.g. Nelson et al. 2019; Schaye et al. 2015; Croton et al. 2016; Gonzalez-Perez et al. 2014), negative feedback from these processes is a required mechanism that helps star formation quenching in the host galaxy, leading to the observed abrupt decrease in the galaxy luminosity function at the high-luminosity end (Silk & Mamon 2012; Naab & Ostriker 2017).

* E-mail: bruno.ddeo@gmail.com

The percentage of the AGN bolometric luminosity (L_{bol}) that couples with the interstellar medium (ISM) of the galaxies – the AGN coupling efficiency – seems to have a minimum threshold for it to have a significant impact on the galaxy (e.g. an outflow that can lead to escape of gas from the gravitational potential of the host galaxy). Using galaxy mergers simulations, [Di Matteo et al. \(2005\)](#) found a threshold of $\sim 5\% L_{\text{bol}}$ in order to reproduce the relation between the mass of the SMBH (M_{SMBH}) and the velocity dispersion σ_* of the galaxy bulge ([Gebhardt et al. 2000](#); [Ferrarese & Merritt 2000](#)). Using empirical estimates of other parameters, [Zubovas \(2018\)](#) also got $5\% L_{\text{bol}}$, but for redshift $z \sim 3$ (with 13% for $z \sim 0.5$). According to the ‘two-stage’ model of [Hopkins & Elvis \(2010\)](#), this percentage could be lower, with a threshold of $0.5\% L_{\text{bol}}$. Note that these efficiencies refer not only to the kinetic power of outflows – that will be studied in this work – but to the total energy released.

In the so-called radiative mode feedback, radiation pressure from the AGN accretion disk leads to the formation of winds that couple with the circumnuclear interstellar medium of the host galaxies leading to outflows observed in the ionized gas of the Narrow-Line Region (e.g. [Storchi-Bergmann et al. 2010](#); [Riffel et al. 2013, 2020](#)). Most of such studies have been done in the optical using the kinematics measured from the $[\text{O III}]\lambda 5007$ emission line (e.g. [Crenshaw & Kraemer 2007](#); [Fischer et al. 2013, 2018](#)). AGNs can also influence the ISM via the radio-mode (or jet-mode) feedback, where radio jets interact with the gas, which can occur even in non radio-loud quasars (e.g. [Villar-Martin et al. 2021](#); [Jarvis et al. 2019](#)). Strong outflow powers, in excess of $0.5\% L_{\text{bol}}$, have been obtained for a few individual sources (e.g. [Cresci et al. 2015](#); [Chen et al. 2019](#); [Couto et al. 2020](#)). The energy released can also couple strongly with the molecular and neutral phase (e.g. [Feruglio et al. 2015](#); [Cicone et al. 2014](#)). Strong outflows have even been seen in the earlier Universe ($z \sim 6$, [Maiolino et al. 2012](#); [Cicone et al. 2015](#)), although this seems not to be common ([Novak et al. 2020](#)).

Regarding the strength of the outflow power \dot{E}_{out} in larger sample compilations covering $10^{44} \leq L_{\text{bol}} \leq 10^{48} \text{ erg s}^{-1}$, [Fiore et al. \(2017\)](#) reported kinetic efficiency $\dot{E}_{\text{out}}/L_{\text{bol}}$ of $0.1\text{--}10\%$ for outflows in the ionized phase, and $1\text{--}10\%$ in the molecular phase, as required by models for a significant impact on the evolution of the host galaxy. Nevertheless, other recent studies (e.g. [Baron & Netzer 2019](#); [Trindade Falcão et al. 2020](#); [Davies et al. 2020](#)) claim much lower powers, at least for AGN luminosities below $L_{\text{bol}} \sim 10^{46} \text{ erg s}^{-1}$.

A recent study by our group ([Storchi-Bergmann et al. 2018](#)) of a sample of 9 QSO 2’s with $L_{\text{bol}} \sim 10^{46} \text{ erg s}^{-1}$ at $z \sim 0.3$ investigated the effect of different calculation methods and assumptions in the values of \dot{E}_{out} on the basis of *Hubble Space Telescope* (*HST*) narrow-band images and integrated spectra of the sources. It was concluded that the use of integrated spectra lead to uncertainties in the calculated AGN kinetic power of up to 3 orders of magnitude (see [Revalski et al. 2018a](#), for a complementary analysis). In order to better constrain the properties used in the calculation of the AGN powers, we have now obtained optical integral field spectroscopy of the above QSO sample. Our goal in the present paper is to revisit and improve the calculations of the AGN powers using this spatially resolved data.

This paper is organized as follows. In [Sec. 2](#) we present

Table 1. Sample. (1) galaxy full name (prefix SDSS); (2) redshift; (3) observed $[\text{O III}]\lambda 5007$ luminosity (in units of $10^{42} \text{ erg s}^{-1}$); (4) spatial scale (in kpc/arcsec); (5) luminosity distance (in Mpc).

SDSS name (1)	z (2)	$L_{[\text{O III}]}$ (3)	Scale (4)	D_L (5)
J082313.50+313203.7 [†]	0.43320	25.0	5.46	2310
J084135.04+010156.3 [†]	0.11045	5.37	1.95	498
J085829.58+441734.7 [†]	0.45395	11.6	5.61	2450
J094521.34+173753.3 [†]	0.12838	6.47	2.22	583
J123006.79+394319.3 [†]	0.40699	21.8	5.26	2149
J135251.21+654113.2 [†]	0.20747	18.8	3.26	980
J155019.95+243238.7 [†]	0.14294	4.83	2.42	653
J120041.39+314746.2 [‡]	0.11586	8.33	2.04	524

HST data from: [†][Storchi-Bergmann et al. \(2018\)](#), [‡][Fischer et al. \(2018\)](#)

the sample, in [Sec. 3](#) we describe the observations and data reduction, in [Sec. 4](#) we describe the analysis methodology, in [Sec. 5](#) we present our results, in [Sec. 6](#) we discuss them and in [Sec. 7](#) we present our conclusions.

2 SAMPLE

Our sample consists of 7 type 2 QSOs from the 9 objects targeted in [Storchi-Bergmann et al. \(2018\)](#) in a study of *Hubble Space Telescope* (*HST*) narrow-band images combined with Sloan Digital Sky Survey (SDSS) spectra. The 9 type 2 QSOs were drawn from the [Reyes et al. \(2008\)](#) sample, selected for having luminosities $L_{[\text{O III}]\lambda 5007}$ above $10^{42} \text{ erg s}^{-1}$, and redshifts in the range $0.1 < z < 0.5$: these are luminous QSOs that could still be well resolved by *HST* imaging observations. To the original sample we added 1 similar object (J120041) from [Fischer et al. \(2018\)](#). Incidentally, most of these galaxies have signs of mergers (see discussion in [Section 6.1](#)) as seen in the *HST* continuum maps ([Fig. 1](#)), which supports previous findings that a high incidence of mergers is correlated with strong nuclear activity (e.g. [Treister et al. 2012](#)).

Some basic information of the sample objects is presented in [Table 1](#): full name identifications (we use short names in the other tables), systemic redshifts (z , see [Section 4.4](#)), $[\text{O III}]\lambda 5007$ total luminosity (from *HST* images), angular scales and luminosity distances (D_L). The angular scale was used to convert spatial distances from arcseconds to kiloparsecs, and D_L to obtain luminosities from fluxes. These two quantities were derived from the redshift, using the cosmological calculator of [Wright \(2006\)](#) with $H_0 = 73 \text{ km s}^{-1}$, $\Omega_M = 0.27$ and $\Omega_\Lambda = 0.7$, with the redshifts corrected for the CMB dipole model ([Fixsen et al. 1996](#)).

3 OBSERVATIONS AND DATA REDUCTION

3.1 Observations

Observations were undertaken with the Integral Field Unit (IFU, [Allington-Smith et al. 2002](#)) of the Multi-Object Spectrographs (GMOS) available at both Gemini telescopes. The details of the observations are displayed in [Table 2](#). The GMOS-IFU fields-of-view of each observation are shown as

green rectangles over the *HST* [O III] narrow-band images in Fig. 1, and the spectra of the sample – integrated over the IFU data cubes – are displayed in Fig. 2.

The GMOS-IFU instrument offers two configurations, depending on how the fibers are arranged: the two-slit mode covers a field-of-view (FoV) of $5'' \times 7''$, and is identified as IFU-2 in the table, while the one-slit mode (IFU-R) has a smaller FoV ($5'' \times 3.5''$) but covers a wider spectral region. For our observations, we opted for the one-slit mode because it enables the observation of more emission lines: from $H\beta$, [O III] $\lambda\lambda 4959, 5007$, to $H\alpha$, [N II] $\lambda\lambda 6548, 84$ and the pair [S II] $\lambda\lambda 6718, 31$. In order to cover these lines and still have an adequate spectral resolution, R400 and B600 gratings were the best choices. When necessary, filters were used to block second-order contamination of the spectra. For each object, several exposures were obtained, aiming to: achieve a signal-to-noise ratio (S/N) above 3 at mid distances between the nucleus and regions at the borders of the IFU FoV; fill the spectral gaps (caused by the gaps between the CCDs) and the spatial holes (caused by dead lenslets/fibers), by means of dithering (offsetting) the observations in the spectral and spatial dimensions, respectively. The total exposure of the combined observations is also shown in the table.

As we found in the Gemini archive similar data for other two nearby QSOs – J085829 and J094521 – we have included also these objects in our analysis to enrich our study. These objects are identified in Table 2 along with the references to the published results.

The archival data does not match all the requirements of our own observations (see Fig. 2). J085829 observations used the two-slit mode (IFU-2), resulting in a much smaller wavelength range, covering only $H\beta$ and the [O III] doublet. In the case of J094521, the use of the B1200 grating, which has a higher resolution, and consequently smaller spectral coverage, also results in a spectrum with only these three emission lines, along with $H\gamma$.

3.2 Data reduction

The data reduction was carried out with the Python package GIREDS¹. This software automatizes the process, organizing the fits files and applying all the standard steps – which include the reduction of both the standard star and the science files – using the IRAF’s (Tody 1986) packages provided by Gemini. The steps include (not in order) bias subtraction, cosmic ray removal and sky subtraction, flat fielding, fiber identification and wavelength calibration.

After the relative flux calibration, the software creates a data cube for each science observation, already corrected for differential atmospheric refraction. Instead of sampling the reduced data using the diameter of the fibers (~ 0.2 arcsec), we over-sampled the pixel scale, setting it to 0.1 arcsec/pixel. Before merging the individual exposures, we removed the telluric absorption contribution from each data cube (see Section B1 in the online supplementary material).

At this step, each galaxy had a set of data cubes spatially offset from each other. Using the instrumental offsets (listed in the header), the software merged all observations into a final data cube, containing the calibrated flux and its

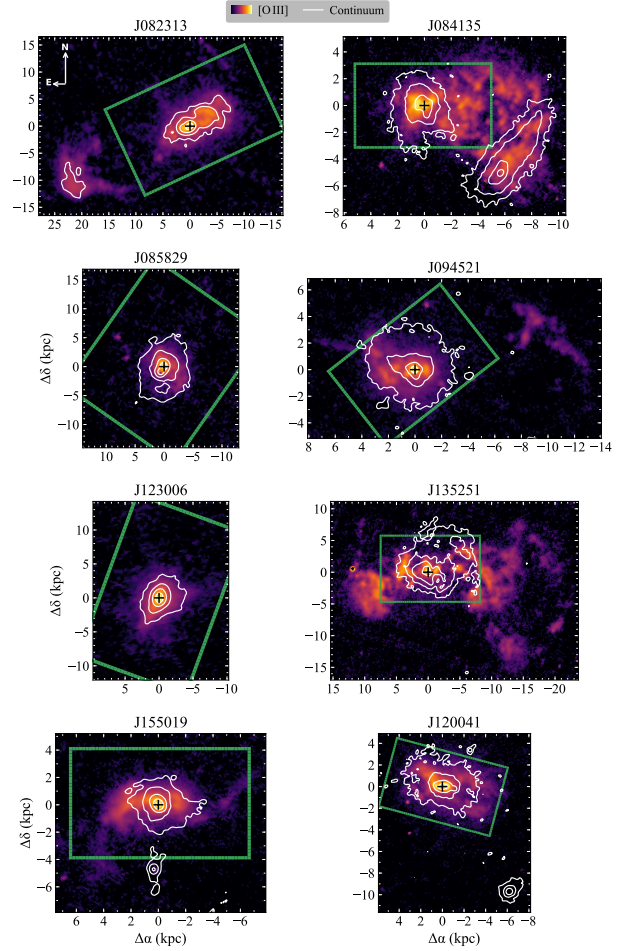


Figure 1. *HST* narrow-band images of our sample. The maps show the [O III] flux distribution of the galaxies, with contours (white) from images of the stellar continuum, both in logarithmic scale. The GMOS-IFU FoVs are highlighted as green rectangles.

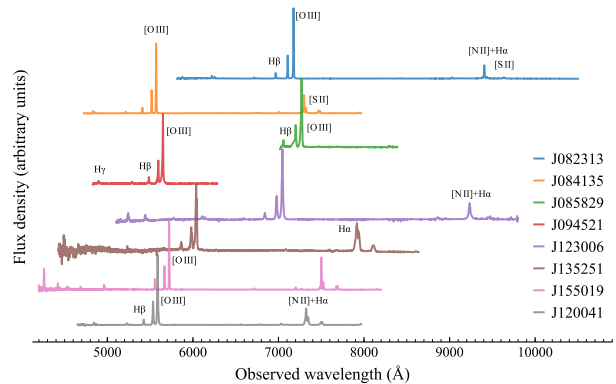


Figure 2. Spectra of the galaxies of our sample, integrated within a seeing-sized radius aperture over the data cube.

¹ <https://github.com/danielrd6/gireds>

Table 2. Observations and reduction. (1) galaxy short name (full name in Table 1); (2) Gemini observation ID; (3) and (4): gratings and filters full names; (5) total exposure time (in seconds); (6) spectral resolution (standard deviation, in Å); (7) FWHM of the PSF (in arcsec), characterising the local seeing; (8) multiplicative factor to the flux calibrated data to match the SDSS spectra flux; (9) instrumental resolution (in km s^{-1}), corresponding to the rest wavelength range 4861.3–6730.8 Å (calculated from column 6).

Name (1)	Observation ID (2)	Grating (3)	Filter (4)	Exptime (5)	Spec. Res. (6)	FWHM _{PSF} (7)	$F_{\text{SDSS}}/F_{\text{GMOS}}$ (8)	σ_{inst} (9)
J082313	GN-2018B-Q-207	R400_G5305	GG455_G0305	6×1040	1.00	0.68	0.42	61.9–44.7
J084135	GS-2018B-Q-110	B600_G5323	open	8×1115	0.636	0.65	0.76	39.2–28.3
J085829	GN-2010B-C-10 [†] *	R400_G5305	i_G0302	2×1800	1.06	0.59	1.14	65.2–47.1
J094521	GS-2010A-Q-8 [‡] *	B1200_G5321	open	4×1300	0.339	0.75	0.89	20.9–15.1
J123006	GN-2019A-Q-228	R400_G5305	GG455_G0305	3×1150	1.05	0.54	0.16	65.0–46.9
J135251	GN-2019A-Q-228	R400_G5305	open	6×900	1.00	0.55	0.61	61.9–44.7
J155019	GN-2018A-Q-206	R400_G5305	open	4×1200	1.03	0.55	0.73	63.3–45.7
J120041	GN-2019A-Q-228	B600_G5307	open	3×1250	0.738	0.72	0.50	45.5–32.9

Data from Gemini Archive, with published results in [†]Liu et al. (2013a), and [‡]Harrison et al. (2014)

* Observed in two-slit mode (IFU-2), while the remaining galaxies used one-slit mode (IFU-R)

uncertainties (propagated from the Poisson statistics of the uncalibrated data). Furthermore, to obtain an absolute flux calibration – so that our fluxes matched the SDSS spectra fluxes – we calculated the flux ratio $F_{\text{SDSS}}/F_{\text{GMOS}}$ (listed in Table 2) and multiplied our data by this factor. This ratio is the average of the flux density ratio, calculated for 10 Å windows, where the GMOS-IFU spectrum is the integrated spectra over the corresponding SDSS or BOSS angular aperture.

The information of the rotation/inversion transformations contained in the World Coordinate System (WCS) were taken from the acquisition images, after scaling them to match the pixel scale of the cubes. The reference pixel CRPIX1,2, corresponding to the IFU continuum maximum, has the right ascension and declination CRVAL1,2 taken from the peak continuum in the *HST* images.

To characterize the local atmospheric seeing, using DAOPHOT package from IRAF, we fitted Moffat functions for the radial profiles of the field stars in the acquisition images. We obtained the full width at half maximum (FWHM) of the instrument point spread functions (PSF) (FWHM_{PSF} in Table 2, for an average Moffat parameter $\beta \sim 3.5$). In this work, we also used $\sigma_{\text{PSF}} = \text{FWHM}_{\text{PSF}}/2.355$ for the standard deviation, although the Moffat profiles deviates from a simple Gaussian.

Along with the integral field spectroscopy data, we made use of the available *HST* data from Storchi-Bergmann et al. (2018); Fischer et al. (2018). They consist of narrow-band images centred on [O III] and H α emission lines, and in the continuum between these two lines (used to subtract its contribution from the emission line images). We also made use of the Sloan Digital Sky Survey (SDSS) spectra, taken from the Data Release 13 (Blanton et al. 2017).

4 METHODOLOGY

4.1 Emission line fitting

The emission lines profiles can be quite complex, showing a superposition of different components. Therefore, in order to retrieve the ionized gas kinematic and excitation information, we proceeded to model the emission lines with multiple Gaussian curves, which are individually characterized by

three parameters: the line-of-sight (LoS) centroid velocity (v , also called radial velocity here); velocity dispersion (σ); and amplitude (A). We are considering that each component is measuring the properties of different groups of clouds along the line-of-sight in each pixel. In our fits, we used up to four Gaussians to model each emission line, adopting the same number of components in all pixels of a given object.

Our goal in the present paper is to quantify the AGN feedback via its kinematic coupling with circumnuclear gas of the host galaxy in the ISM. This coupling leads to disturbances in the gas kinematics, the highest velocity ones being observed in the profile wings. We assume that the broad (b) component is tracing this disturbance and calculate the associated feedback which is usually identified as being due to AGN outflows. We note that this approach may have limitations (see discussion in Section 6.1.2), as is probably the case of J094521, that may have a second ‘outflowing component’ (see Section 6.4).

We thus impose that, for every pixel, the broad component should always have the largest σ . The remaining components are called **narrow**s (n1, n2, ..), which we assume that are originated in clouds that are not kinetically disturbed by an outflow. In our sample, the majority of the QSOs have signs of interactions in the *HST* continuum images (see contours in Fig 1, and the discussion in Section 6.1). Hence, the **narrow** components may be not only modelling or tracing the less disturbed gas in the the galaxy, but possibly also the gas from the two different galaxies involved in the interaction, with initial non-zero relative velocities. Possibly because of this, we needed to use more than one narrow component in half of our galaxies, since there are regions where we clearly cannot model their emission lines with only one **narrow** and one **broad** component (see Fig. 3).

We fitted simultaneously the following emission lines, using the same number of **narrow** and **broad** components for each line: H β , [O III] $\lambda\lambda$ 4959,5007, H α , [N II] $\lambda\lambda$ 6548,84 and [S II] $\lambda\lambda$ 6718,31. For J094521, we also fitted H γ , used later to obtain its reddening in Section 4.2.2.

We defined groups of components that are forced to have the same kinematic properties (centroid velocities v and velocity dispersions σ) for all emission lines (in units of km s^{-1}): $\sigma_{\text{H}\beta,\text{b}} = \dots = \sigma_{[\text{S II}],\text{b}}$; and $v_{\text{H}\beta,\text{b}} = \dots = v_{[\text{S II}],\text{b}}$, and equivalently for each **narrow** component. The velocity dis-

persion σ_x refers to the observed value ($\sigma_{x,obs}$) corrected by the broadening caused by the instrumental dispersion (σ_{inst}): $\sigma_{H\alpha}^2 = \sigma_{obs,H\alpha}^2 - \sigma_{inst,H\alpha}^2$. Note that σ_{inst} (in km s^{-1}) is different for each emission line rest wavelength (see Table 2). This correction is based on the one presented by Gallagher et al. (2019).

To decrease the number of fitting parameters, we fixed the ratios between doublet lines according to their expected ratios (Osterbrock & Ferland 2006): $[\text{O III}]\lambda\lambda 5007/4959 = 3$ and $[\text{N II}]\lambda\lambda 6584/6548 = 3$. We also added the following flux constraints, to avoid non-physical solutions: $\text{H}\alpha/\text{H}\beta > 2.74$ (intrinsic recombination value for $T_e = 2 \times 10^4 \text{ K}$ and $n_e = 10^2 \text{ cm}^{-3}$, also according to Osterbrock & Ferland (2006), and $0.436 < [\text{S II}]\lambda\lambda 6718/6731 < 1.496$ (asymptotic values for high and low densities from Proxauf et al. 2014). These bounds/constraints were applied to each component.

The fitting procedure was performed using the publicly available software IFSCUBE (Ruschel-Dutra 2020). This program uses SCIPY (Virtanen et al. 2020) implementations of non-linear minimization and allows the addition of constraints and bounds to the parameters. For each spectrum, the chi-square of the difference between the observed and the modelled flux densities is minimized, where the flux uncertainties and degrees of freedom are considered. Initially, a guess to the parameters of an initial pixel is given. Then, the program fits the rest of the pixels, updating the initial guess based on the successful fits of the neighbouring spectra.

4.1.1 Constraining the number of components

To obtain the number of the components needed to fit the emission lines, first, we fitted only the $[\text{O III}]\lambda\lambda 4959,5007$ emission lines, due to their high S/N. We varied the initial parameter guesses, trying to keep the spatial continuity in the resulting maps of the parameter.

Next, we ran the fitting procedure for all emission lines simultaneously. However, depending on the region, some components may be very weak. Therefore, we started the new fit in a high S/N pixel, that displayed all components, using the resulting parameters (kinetic part) of the previous $[\text{O III}]$ fit as the new initial guesses.

In Fig. 3, we present results of the fitting process for representative $[\text{O III}]$ emission-line profiles of each QSO, with the Gaussian profiles superimposed on the original spectra. Along with the broad, four QSOs needed more than one narrow component in the models: J084135, J094521, J135251 and J120041. Examples of fits of profiles from other spaxels are displayed for J135251 in Fig. 4, while the corresponding figures of the remaining QSOs are presented in the online supplementary material (Figs. B6–B13), where different rows correspond to line profiles from different spaxels over the FoV, with the columns displaying a zoom-in on the emission line profiles of $\text{H}\beta$, $[\text{O III}]$, $[\text{N II}]$, $\text{H}\alpha$ and $[\text{S II}]$. We chose to show pixels with different characteristics, highlighting the fact that the number of components needed in the models may vary over the FoV. For example, J094521 (Fig. B9) has a low- σ component (narrow1) that is only visible away in pixels outside the nuclear region (mainly at $\sim 3 \text{ kpc}$ to the East, as it can also be seen in the maps of Fig. A4). We can also observe that the multiple components appear not only in $[\text{O III}]$, but also in the other emission lines (e.g. first row of

Fig. 4, for J135251). This reinforces the decision of fixing the kinematics among components of different emission lines.

During the profile fitting process, we identified that the nuclear spectra of J082313 were best fitted using an additional (weak) Broad Line Region component to the $\text{H}\alpha$ emission line profiles (see Section B2 in the online supplementary material).

4.2 Gas excitation and physical properties

From the emission-line ratios, we have checked the gas excitation over the whole emitting regions via the BPT diagram (Baldwin et al. 1981) that is presented in the online supplementary material (Section B3). This diagram shows a range of $[\text{N II}]/\text{H}\alpha$ ratios but high $[\text{O III}]/\text{H}\beta$ ratios everywhere putting all points in the Seyfert excitation region.

4.2.1 Density

In order to obtain a measurement of the electron density (n_e), we have first used the ratio between the pair of lines $[\text{S II}]\lambda\lambda 6718,31$. Assuming a typical NLR electron temperature in AGNs of $T_e = 10^4 \text{ K}$, we obtained n_e following Proxauf et al. (2014). The two objects – J085829 and J094521 – that didn't have $[\text{S II}]$ coverage in the IFS spectra, had n_e measured from the the SDSS spectra. The resulting n_e values as a function of radial distance from the nucleus are shown in Fig. 5. Whenever possible, we performed two calculations for n_e : using only the broad components ($n_{e,[S II]b}$, in orange), and using the integrated profile comprising all components ($n_{e,[S II]n+b}$, in blue). Both values display significant uncertainties due to the closeness of the lines and their multiple components (e.g. Fig. 4), with the broad one being more affected due to its lower S/N. Since the resulting $n_{e,[S II]n+b}$ and $n_{e,[S II]b}$ values are consistent within the errors, we were not able to verify if $n_{e,[S II]b} > n_{e,[S II]n+b}$, as found by other authors (e.g. Villar Martín et al. 2014). Therefore, due to its lower variance and higher spacial coverage, we decided to use $n_{e,[S II]n+b}$ in the calculations with the method we have called 'default' along this paper. In the following sections we define the other assumptions and parameters of this default method (see Table 5). Figs. 6 and A1–A7 show the spatial distribution of $n_{e,[S II]n+b}$ for all targets.

Proxauf et al. (2014) updated the expression for another electron density tracer, the $[\text{Ar IV}]\lambda\lambda 4711,40$ emission-line ratio, which is best suited to calculate the gas density associated with the $[\text{O III}]$ emitting clouds due to the more similar ionization potential than that of the $[\text{S II}]$ lines (see discussion in Section 6.5.5). Using a PSF-size aperture spectra, we could measure these lines for two objects (J082313 and J084135) which show in the spectra $[\text{Ar IV}]$ lines with $\text{S/N} > 3$. We fitted these lines with a Montecarlo method (see Section B4 in the online material), obtaining higher $n_{e,[Ar IV]}$ values than those obtained from the $[\text{S II}]$ lines (red errorbars in Fig. 5).

Finally, we have also investigated the method of calculation of the gas density described in Baron & Netzer (2019, BN19), which is based on the ionization parameter U . We calculated U using their expression, that depends on the line ratios of $[\text{O III}]/\text{H}\beta$ and $\text{H}\alpha/[\text{N II}]$ (obtained from SDSS, in the case of J085829 and J094521). The equation depends

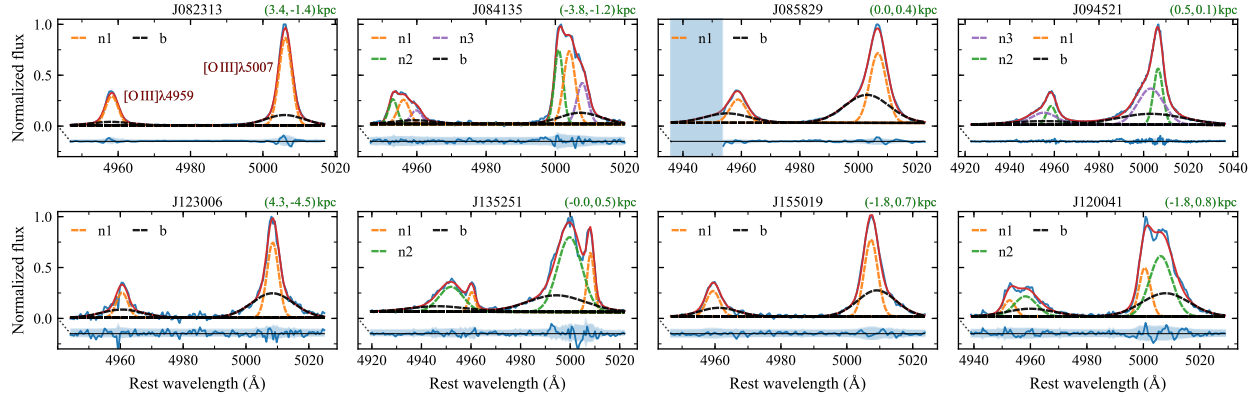


Figure 3. Examples of fitting results for the [O III] line profiles for each galaxy of the sample, highlighting the decomposition of the spectral flux density in narrow (n1, n2, n3) and broad (b) components. The pixel location (projected distance from the nucleus, in kpc) is shown in top right of each panel. Four objects have more than one narrow component, clearly seen in both [O III] profiles. Here, J094521 does not show its n1 component, that appears in another region of the galaxy, away from the nucleus (see Fig. A4, and Fig. B9 in the online material). An alternative and larger version of this figure is available in the online material (Fig. B5).

also on the AGN bolometric luminosity (L_{bol}), and the extent of the region associated with the outflow R_{out} , with a $n_{e,\text{BN19}} \propto L_{\text{bol}} U^{-1} R_{\text{out}}^{-2}$ dependence. Fig. 5 displays the values calculated for different radii, separated by a FWHM_{PSF} width (black dotted bars). L_{bol} (Table 3) were calculated in Storchi-Bergmann et al. (2018), from the Trump et al. (2015) relation between L_{bol} and the reddening-corrected (Lamatra et al. 2009) [O III] $\lambda 5007$ luminosity (Table 1 displays the values before the reddening correction). For J120041 (that is not in Storchi-Bergmann et al. (2018) sample), we applied the same method. In Section 6.5.5, we discuss the effect that different density tracers have in the outflow properties.

4.2.2 Reddening

To measure the extinction caused by foreground dust, we compared the observed ratio of hydrogen Balmer emission lines with its intrinsic recombination value for a given electron temperature and density, assuming the same reddening value for all the components. The color excess $E(B-V)$ was obtained using the expression from Revalski et al. (2018a), where $R_{\text{H}\alpha}$ and $R_{\text{H}\beta}$ were obtained from the reddening law of Savage & Mathis (1979). Assuming that the extinction is the same to all components, the observed ratio $(\text{H}\alpha/\text{H}\beta)_{\text{obs}}$ was computed using the sum of the fluxes of all components of each emission line, while the intrinsic value was set to $(\text{H}\alpha/\text{H}\beta)_{\text{int}} = 3.1$ (Halpern & Steiner 1983). To obtain the corrected absolute flux from a given emission line, we used $F(\lambda)_{\text{int}} = F(\lambda)_{\text{obs}} \cdot 10^{0.4 R_{\lambda} E(B-V)}$ (Seaton 1979), with $F(\lambda)_{\text{obs}}$ and $F(\lambda)_{\text{int}}$ being the observed and the corrected fluxes, respectively, of a given emission line, with R_{λ} also obtained from Savage & Mathis (1979). For J094521, we used instead the ratio $\text{H}\gamma/\text{H}\beta$, because its spectra do not cover the $\text{H}\alpha$ region (see Fig. 2), using an intrinsic value $(\text{H}\gamma/\text{H}\beta)_{\text{int}} = 0.469$ (Osterbrock & Ferland 2006, case B, $T_e = 10^4$ K) in this case. The spacial distributions are shown in Figs. 6, and A1–A7. For J085829, we used a single value of $E(B-V) = 0.27$ mag, obtained from the SDSS spectrum.

4.3 Ionized gas mass

The mass of the ionized gas ($M_{\text{H II}}$) can be obtained from the luminosity of H II emission lines. Ignoring the small contribution from ions other than H II and He II to the total gas mass, we can use (Storchi-Bergmann et al. 2018):

$$M_{\text{H II}} = \frac{(1.4 m_p) L(\text{H}\beta)}{n_e \alpha_{\text{H}\beta}^{\text{eff}} (h\nu_{\text{H}\beta})}, \quad (1)$$

where m_p is the proton mass, $L(\text{H}\beta)$ is the $\text{H}\beta$ luminosity (calculated from its flux and D_L from Table 1), $h\nu_{\text{H}\beta}$ is the energy of the transition, $\alpha_{\text{H}\beta}^{\text{eff}} = 3.02 \times 10^{-14} \text{ cm}^3 \text{ s}^{-1}$ is the effective recombination coefficient of $\text{H}\beta$ (for $n_e = 10^2 \text{ cm}^{-3}$, and $T_e = 10^4$ K). The factor 1.4 is to consider the contribution of He to the total mass. $\text{H}\alpha$ has a higher S/N over most of the FoV, covering a larger spatial extent. Therefore, instead of directly using the $\text{H}\beta$ luminosity, we used the $\text{H}\alpha$ luminosity: $L_{\text{H}\beta} = L_{\text{H}\alpha}/3.1$ (based on the intrinsic ratio assumed in the reddening correction). However, we used $\text{H}\beta$ in J085829 and J094521, since their spectra do not cover the $\text{H}\alpha$ line (see Fig. 2).

4.4 Outflow velocity

We made the hypothesis that the broad component is tracing the outflow. In order to weight in particular the effect of the highest velocity gas that contributes to the wings of the emission line profile, we used the following parametrization for the outflow velocity (v_{out}):

$$v_{95} = |v_{\text{broad}}| + 2 \sigma_{\text{broad}}, \quad (2)$$

where v_{broad} is the centroid velocity (velocity shift relative to the galaxy systemic velocity) of the broad component, and σ_{broad} its velocity dispersion. This definition is similar to V_{max} from Rupke & Veilleux (2013); Fiore et al. (2017). In this equation, we are assigning values of velocity at the extreme ends of the broad component as representative of the outflow velocity. In Section 6.5, we test other v_{out} definitions.

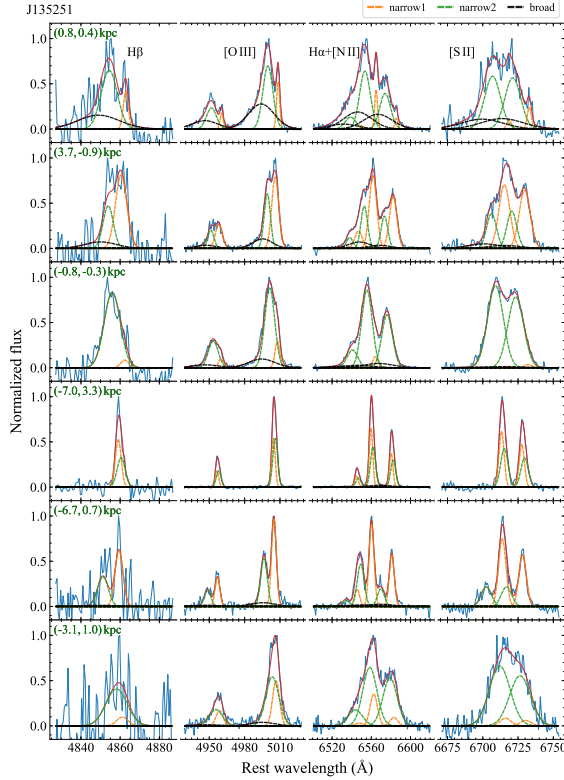


Figure 4. Fitting results for a few spectra of J135251. Each row of the figure corresponds to a different position in the galaxy, identified by $(\Delta\alpha, \Delta\delta)$, the distance from the nucleus (in green at the upper left corner of each row). The columns are zoom in the emission lines: $H\beta$, $[O\text{ III}]$, $(H\alpha + [N\text{ II}])$ and $[S\text{ II}]$.

The galaxy systemic velocity was adopted to correspond to the mean value of one of the **narrow** components, inside a seeing-size radius: **narrow1** for most galaxies and **narrow2** for J094521 and J120041. The criterion used for this assumption was to consider as systemic, the component that best represents the velocity field of the host galaxy, that we assumed to be the component with lowest mean velocity dispersion inside this region, as broader components may contain, for example, contribution from outflows or gas from interacting companion galaxies. In this way we avoid adopting as systemic velocity those from components that are not present in the galaxy nucleus (e.g. n1 in J094251, as shown in Fig. A4). Table 1 displays the corresponding systemic redshifts.

The fitting process imposed that the **broad** components of all emission lines from a given spectrum have the same kinematics, hence we could use any emission line to calculate v_{out} . We chose $[O\text{ III}]\lambda 5007$ because its higher S/N ratio over the FoV (in relation to the other lines), allows its measurement up to larger distances from the nucleus.

4.5 Mass outflow rate and power

In order to characterize the feedback, we obtained the ionized gas mass outflow rate ($\dot{M}_{out}(r)$) and the outflow power ($\dot{E}_{out}(r)$) as a function of radial distance from the nucleus. These quantities were calculated as rates crossing rings at

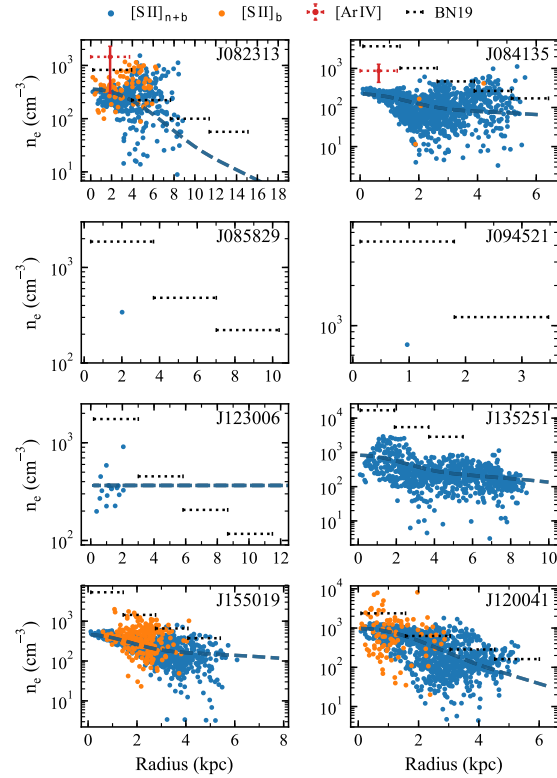


Figure 5. Comparison of gas density values obtained from different indicators. Orange circles were obtained using only the **broad** component of the $[S\text{ II}]$ lines, while blue circles were obtained from the integrated profiles (n+b). In red, the values obtained from the $[Ar\text{ IV}]$ lines in seeing-size aperture spectra. Also shown are values from the ionization parameter method (Baron & Netzer 2019, BN19), for successively increasing radii (black dotted bars). The dashed blue lines are the fits made to $n_{e,[S\text{ II}]_{n+b}}$ (see Section 4.6). J085829 and J094521 have $n_{e,[S\text{ II}]_{n+b}}$ measured from their SDSS spectra.

increasing radii r from the nucleus. Following Shimizu et al. (2019), we define:

$$\dot{M}_{out}(r) = \frac{M_{H\text{ II}}(r)v_{out}(r)}{\delta r}, \quad (3)$$

$$\dot{E}_{out}(r) = \frac{1}{2}\dot{M}_{out}(r)v_{out}^2(r), \quad (4)$$

where δr is the width of an annular aperture, at a given radius r with origin at the nucleus. The position of the nucleus was adopted to correspond to the peak of the continuum emission, while $\delta r = 0.5\sigma_{\text{PSF}}$ (where $\sigma_{\text{PSF}} = \text{FWHM}_{\text{PSF}}/2.355$). $M_{H\text{ II}}(r)$ is the integration of $M_{H\text{ II}}(x,y)$ over all pixels inside each δr annulus, while the $v_{out}(r)$ is the average velocity value within the annulus (see Fig. 12).

In the **default** method, $M_{H\text{ II}}$ (Eq. 3) was calculated using only the **broad** component, adopted to correspond to the outflowing gas. However, we tested the effect of using all components (**broad+narrow**) in Section 6.5.2. The above equations imply that we are observing the v_{out} component

that radially crosses each annulus, but we are actually measuring only the line-of-sight component of v_{out} and the sky-plane component of δr . In Section 6.5.3, we discuss how the projection effects in v_{out} and δr affect the calculations.

4.6 Signal-to-noise ratio

For each component, we only used pixels with $S/N > 3$, where the signal (S) is the peak flux emission and the value of the noise (N) has been adopted as the standard deviation of the continuum flux close to each emission line. The result is that some data is discarded, limiting the spatial extent of the components measurements. However, in this way we can be more confident on the properties derived from the remaining data. Another issue is that each emission line has a different S/N over the FoV and consequently covers a different extent. For example, there are regions in which $[O\text{III}]\lambda 5007$ is strong, but the gas density could not be determined. Therefore, to compute \dot{M}_{out} and \dot{E}_{out} in these regions, we extrapolated the values of n_e , $E(B-V)$, $F_{H\alpha}$ and $F_{H\beta}$. This was done by modeling the radial profiles of these quantities via the fit of two 1D Gaussian curves over the corresponding radial profiles and replacing the missing values by the ones extrapolated using this model. As an example, Fig 5 shows the resulting fits for $n_{e,[S\text{II}]}$ (for J123006, we used the average).

5 RESULTS

5.1 Maps

We present the result of the fitting process, with maps of the fitted parameters displayed in Fig. 6 for J135251, and Figs. A1–A7 for the remaining QSOs (Larger size versions are available in the online material, Figs. B14–B21). The continuum flux densities were measured in 400\AA wide spectral windows centred at $\lambda 5300\text{\AA}$. We chose to show only the maps for $[O\text{III}]\lambda 5007$ because they have the highest S/N over the whole FoV, and the kinematics of the other emission lines are the same – as imposed by the fitting procedure.

5.2 Outflow radius

In order to investigate the extent of the outflowing component, in Fig. 7 we present the flux density radial profiles of $[O\text{III}]$, both for the **broad** and **narrow+broad** components. The radial profiles correspond to the mean azimuthal value of $F_{[O\text{III}]}$ inside annuli with $\sigma_{\text{PSF}}/2$ width, with the shaded regions showing the standard deviation of the mean. Note that the variation is not the $F_{[O\text{III}]}$ uncertainty, but mostly reflects its variation over the pixels inside each annulus: there are fewer pixels close to the nucleus and at the outer parts of FoV, resulting in a smaller $F_{[O\text{III}]}$ standard deviation. Isolated pixels were discarded, avoiding spurious data, that could lead to an overestimation of the outflow radii.

We measured the radial extent of each component (Table 3), defining the radius R as the maximum radial distance reached, including only pixels with $F_{[O\text{III}]} S/N > 3$ (see profiles in Fig 7). Both R_b and R_{n+b} uncertainties were set equal to σ_{PSF} . Note that some galaxies have these measurements

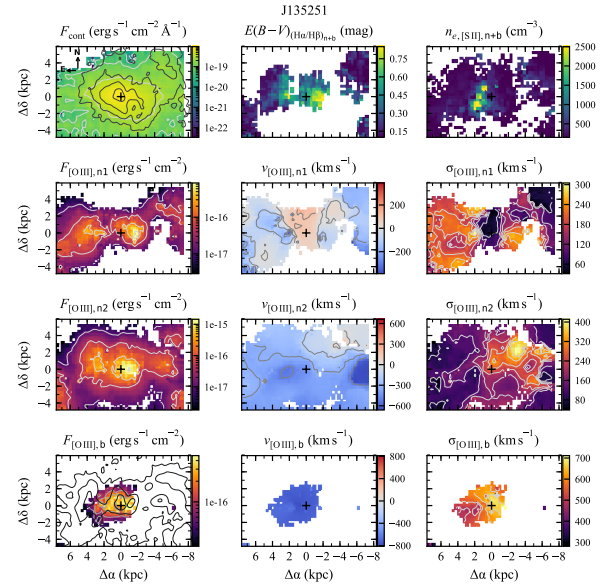


Figure 6. Maps of the measured properties of J135251. In the first row, from left to right, we show: the continuum flux (F_{cont}), the gas reddening ($E(B-V)$), and the electron density (n_e) maps. The remaining rows display maps of the parameters of each $[O\text{III}]\lambda 5007$ component: flux ($F_{[O\text{III}]}$, left); radial velocity ($v_{[O\text{III}]}$, centre); and the velocity dispersion ($\sigma_{[O\text{III}]}$, right column). The last row refers to the **broad** component, while the remaining middle rows refer to the **narrow** components (n1 and n2, in this case). We overplotted the *HST* contours (in black, starting in $3\sigma_{\text{sky}}^{\text{HST}}$) of the continuum (top left) and $[O\text{III}]$ (bottom left) images. North is up and East is left, with the right ascension and declination distances given relative to the continuum peak (black cross). The systemic velocity were calculated from $v_{[O\text{III}],n1}$.

limited by the GMOS-IFU FoV (green region in the figure, and marked by \dagger) in Table 3).

In order to compare the radial extent obtained above with those obtained using the narrow-band images of Storch-Bergmann et al. (2018), we re-measured the $[O\text{III}]$ flux distribution extents in the *HST* images ($R_{[O\text{III}]}$), defining them as the maximum distance from the nucleus where the corresponding fluxes could be measured, limited by the contours at $3\sigma_{\text{sky}}^{\text{HST}}$, where $\sigma_{\text{sky}}^{\text{HST}}$ is the flux standard deviation in a region of sky. These are shown as the outermost black contours in the lower left panel of Figs. 6 and A1–A7, although it is not completely visible in some galaxies (due to the small IFU FoV, as shown in Fig. 1). The $R_{[O\text{III}]}$ uncertainties are equal to the difference in the extent values measured at the thresholds corresponding to 2 and $4\sigma_{\text{sky}}^{\text{HST}}$. The above radial sizes are also shown in Table 3.

5.3 Radial profiles of \dot{M}_{out} and \dot{E}_{out}

Using Eqs. 3 and 4, we obtained radial profiles of $\dot{M}_{out}(r)$ and $\dot{E}_{out}(r)$ for the galaxies in our sample. Fig. 8 shows the rates of these quantities crossing $\delta r = \sigma_{\text{PSF}}/2$ wide rings, at different radii r . As described in Section 4.5, the outflow velocity $v_{out}(r)$ is the mean value calculated from $v_{out}(x,y)$

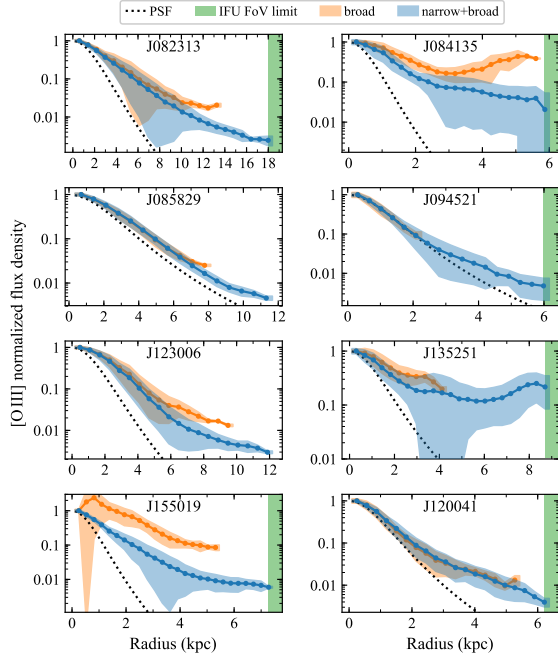


Figure 7. Radial profiles of the normalized [O III] flux density, both for the **broad** and **narrow+broads** components. The blue line is the mean value of $F_{[\text{O III}],n+b}$, inside annuli $\sigma_{\text{PSF}}/2$ wide, while the orange line is calculated from $F_{[\text{O III],b}}$. The shaded regions are the $F_{[\text{O III}]}$ standard deviation of the azimuthal mean value. The R_b and R_{n+b} extents in Table 3 correspond to the radial profiles limits. The green vertical regions mark the limit of the IFU FoV, and the black dotted line is the PSF radial profile.

within the annuli, and $M_{\text{H II}}(r)$, the sum of $M_{\text{H II}}(x,y)$ along the annuli.

More specifically, the figure shows the profiles resulting from our **default** assumptions, namely: ionized gas mass $M_{\text{H II}}^{\text{p}}$, calculated using only the outflow contribution (the **broad** component); electron density $n_{e,[\text{S II}],n+b}$, calculated from the [S II] ratio, using the full profile (**narrow+broads**, see Section 4.2.1); outflow velocity v_{95} (see Section 4.4). Note, however, that the **default** assumptions are not necessarily the best choice. For example, the use of [S II] lines ratios as electron density estimators have been questioned by other authors (e.g. Davies et al. 2020). In order to take these aspects into account, we test the effects of different assumptions in Section 6.5.

We present ‘characteristic’ M_{out} and \dot{E}_{out} values – defined as the maximum values along the corresponding radial profiles (stars in Fig. 8) – following what has been also adopted by other authors (e.g. Shimizu et al. 2019; Trindade Falcão et al. 2020) in Table 3. In this table, we list the values for the **default** assumptions, together with the minimum and maximum values obtained for these properties according to the tests discussed in Section 6.5.

6 DISCUSSION

6.1 Maps

6.1.1 Multiple components and interactions

Diverse and complex scenarios are seen in the maps of the flux distributions and kinematics of the ionized gas from our galaxies (Fig. 6 and A1–A7). Besides the **broad** component, present in all QSOs, 4 of them needed more than one **narrow** Gaussian in order to model its emission-line profiles (see Section 4.1): J084135, J094521, J135251 and J120041. This could be a consequence of the high incidence of mergers in our objects, given that most show signs of interaction in their *HST* images (Fig. 1). The superposition of emission from gas with origin in different galaxies – that have a non-zero relative velocity – and their perturbation from the merger, can lead to more than one **narrow** component.

In J084135 and J135251, besides the highly disturbed ionized gas (mapped by [O III]), we can see the remains of another galaxy in the continuum maps of (Fig. 1), probably the result of a major merger.

J155019 and J120041 have continuum blobs to the South and Southwest of the nucleus, respectively, possibly signaling companions (assuming the same redshift) – that along with the disturbed [O III] (including tidal features in J155019) – suggests a minor merger. In the case of J085829, the only signature of interaction seems to be a second continuum peak, (~ 1.1 kpc to the southeast of the nucleus), suggesting that the interaction is close to settling.

Fig. 1 shows that the [O III] emission of J094521 extends beyond the body of its host galaxy. Using additional *HST* observations of this QSO, Villar-Martín et al. (2021, Fig. A10) pointed out the presence of a huge tidal tail, confirming the existence of an interaction.

J082313 has [O III] and continuum emission to the south-east detached from the main body of the galaxy. The continuum flux distribution could indicate an interacting companion, but the broadband filter of our *HST* observations (see Storchi-Bergmann et al. 2018) is contaminated by the [O III] lines – the same being true for J085829 – and therefore we are not sure about the actual contribution from stars. In addition, the J082313 GMOS-IFS continuum – regardless of its weak S/N – seems to be not totally correlated with the *HST* one (black contours in the upper left panel of Fig. A1), weakening the merger hypothesis.

Therefore, only J123006 and J082313 (and possibly J085829) do not have signs of interactions, and the three of them needed only one **narrow** component for the fit, supporting that the second (an third) narrow components are associated with interactions.

We have found that each component can be quite complex and requires a detailed analysis. But it is not the purpose of the present work to dissect the results of each component – we save that for a future work. As an example, the **narrow1** component of J094521 (Fig A4) has a very low velocity dispersion, and is visible only outside the nucleus. Interestingly, high spatial resolution VLA and e-MERLIN radio maps of this QSO, presented by Jarvis et al. (2019), seem to correlate with the flux distributions of our **narrow1** component. The interpretation that these authors propose is that the radio jet is being deflected while it pushes a cloud of gas (although they didn’t decompose the [O III] profile in

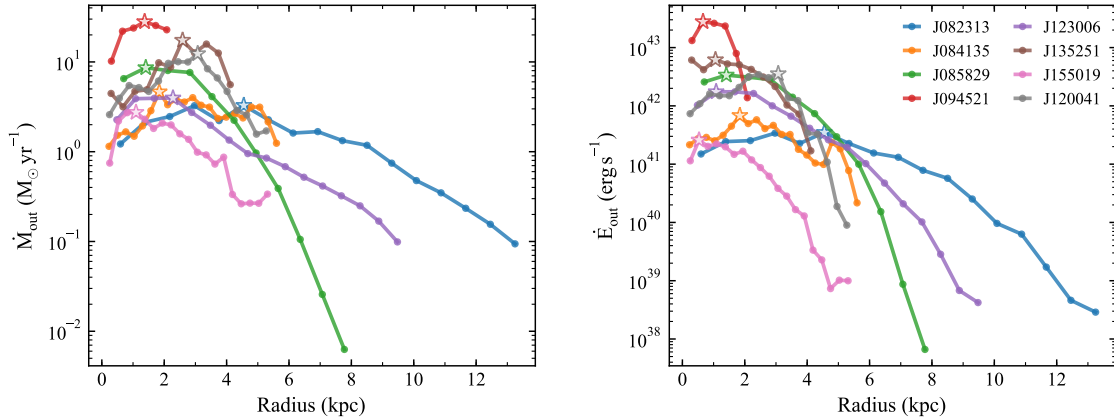


Figure 8. Radial profiles of $\dot{M}_{out}(r)$ (left) and $\dot{E}_{out}(r)$ (right) for the QSOs of our sample. The peak values are highlighted by stars, and correspond to \dot{M}_{out}^{def} and \dot{E}_{out}^{def} listed in Table 3, and presented in Fig. 10 as filled blue stars.

multiple components). The connection between our **narrowl** component and the local radio emission reinforces our results and the need of multiple Gaussian components, which can originate not only in outflows and mergers, as discussed above, but also in interactions with a radio jet.

6.1.2 The broad component

As previously pointed out, the **broad** component is assumed to be tracing the kinematic coupling between the AGN and the host galaxy, which we are generally referring to as ‘outflows’. Here, we analyse its characteristics.

The velocity dispersion maps of the **broad** component ($\sigma_{[O\ III]b}$) show values reaching a maximum of $\sim 900\text{ km s}^{-1}$ for J094521, while in J084135 it reaches only 300 km s^{-1} . The remaining galaxies achieve $\sigma_{[O\ III]b}$ peak values between 400 km s^{-1} and 700 km s^{-1} . The different degrees of disturbance for each object, as revealed by these values, indicates that the feedback is not equally strong for different objects and/or may vary due to varying outflow axis orientation relative to the LoS in an ambient affected by extinction (Bae & Woo 2016).

Part of the sample has radial velocity maps ($v_{[O\ III]b}$) with a predominance of negative values (J085829, J094521 and J135251). This is expected in a scenario where the outflow axis makes a relatively large angle with the plane of the sky, since the radiation coming from the receding part of the outflow should be more affected by dust extinction (Bae & Woo 2016). In particular, this component in J085829, J094521, and J120041 is barely – or not (in the second case) – spatially resolved (compare the spatial profile of $F_{[O\ III]b}$ with that of the PSF in Fig. 7). Along with the negative velocity values of J085829 and J094521, this is a sign that the outflow axes of these two QSOs are more aligned with our LoS (high inclination i relative to the plane of the sky) than the other targets.

On the other hand, J123006 has only positive velocity values, ranging between $\sim 10\text{ km s}^{-1}$ in the most perturbed region, and 100 km s^{-1} in the least perturbed one. Therefore, the region with characteristics of an outflow (higher

$\sigma_{[O\ III]b}$) has velocities close to zero. But this may be due to uncertainties in the calculation of its systemic velocity.

Other QSOs – J082313, J084135, J155019 and J120041 – have a mix of positive and negative velocities, with $|v_{[O\ III]b}|$ maxima between $\sim 80 - 200\text{ km s}^{-1}$. Radial velocity values centred on zero – specially if the velocity field has a small velocity range – can be the result of an outflow axis more aligned with the plane of the sky (small inclination i). We note that our outflow definition includes not only the AGN winds, but also gas that is only moderately disturbed by it without changing significantly its original bulk motion. The scenario is analogous to the ‘disturbed rotation’ discussed by Fischer et al. (2018), where it was used a $\text{FWHM}_{[O\ III]b} > 250\text{ km s}^{-1}$ threshold to identify disturbed gas in interacting systems (Bellocchi et al. 2013; Ramos Almeida et al. 2017). In almost all spaxels of our sample, this threshold is achieved.

Another possible source of disturbance in the gas kinematics is the interaction with a radio jet. Although our sample comprises essentially radio-quiet objects, Villar-Martín et al. (2021) has recently presented VLA radio maps of J094521 and J084135, showing a correlation between the $[O\ III]$ extended emission and the VLA radio maps, revealing that in these galaxies the radio emission probably plays a role in the gas kinematics.

Let’s also consider the possibility that our hypothesis is not correct and the **broad** component – at least in a percentage of the pixels fitted – could be tracing gas that is not in outflow (e.g. gas perturbed by mergers). We indeed observe regions inside the galaxies that have lower $\sigma_{[O\ III]b}$. For example, J155019 (see Fig. A5) has a more perturbed region with $\sigma_{[O\ III]b}$ close to 500 km s^{-1} , while having values $\sim 100\text{ km s}^{-1}$ perpendicular to what seems to be its outflow axis. These less perturbed regions usually appear in spectra with lower S/N of $F_{[O\ III]b}$ (which makes the emission line decomposition harder). A consequence of the weaker intensity, is that associated flux introduces a small effect in the calculations of \dot{M}_{out} and \dot{E}_{out} , although affecting the extent measurements.

Table 3. Outflow properties. Radial sizes (R) in units of kpc, mass outflow rates (\dot{E}_{out}) in units of $M_{\odot} \text{ yr}^{-1}$, outflow powers (\dot{E}_{out}) in units of $10^{42} \text{ erg s}^{-1}$ and kinetic coupling efficiency ($\epsilon_f = \dot{E}_{out}/L_{bol}$) in %. (2)–(3) Radius of the **broad** and **narrow+broad** components, from the GMOS-IFS (see Fig. 7); (4) [O III] radius, from the *HST* images (see Section 5.2); (5) bolometric luminosity (in units of $10^{45} \text{ erg s}^{-1}$); (6)–(8) Peak mass outflow rate, power, and kinetic coupling efficiency, using the **default** assumptions; (9)–(11) Corresponding range of results from the tests with summary in Table 5, and data in Tables 6 and 7.

Name (1)	GMOS-IFS		<i>HST</i>	$\log(L_{bol})$ (5)	default			tests range		
	R_b (2)	R_{n+b} (3)	$R_{[OIII]}$ (4)		\dot{M}_{out}^{def} (6)	\dot{E}_{out}^{def} (7)	ϵ_f^{def} (8)	\dot{M}_{out} (9)	\dot{E}_{out} (10)	ϵ_f (11)
J082313	13.3±1.6	18±1.6*	26.3±1.4	46.7	3.3	0.35	0.0007	[0.22, 8.6]	[0.023, 0.91]	[0.00005, 0.002]
J084135	5.6±0.5	5.9±0.5*	9.3±0.8	45.9	4.6	0.68	0.009	[0.27, 24]	[0.049, 3.7]	[0.0006, 0.05]
J085829	7.8±1.4 [‡]	11.3±1.4	5.4±0.8	46.3	8.6	3.4	0.02	[1.7, 16]	[0.65, 13]	[0.003, 0.07]
J094521	<2.1±0.7 [†]	6±0.7*	12.7±0.8	45.8	28	28	0.4	[7.3, 360]	[4.7, 460]	[0.07, 7]
J123006	9.5±1.2	11.9±1.2	6.2±1.2	46.6	4	1.7	0.004	[1, 7.6]	[0.25, 3.3]	[0.0008, 0.01]
J135251	4.1±0.8	8.7±0.8*	19.3±1.8	46.6	17	6.2	0.01	[0.53, 71]	[0.27, 52]	[0.002, 0.3]
J155019	5.3±0.6	7.3±0.6*	6.5±1.7	45.7	2.7	0.26	0.005	[0.49, 12]	[0.041, 1.9]	[0.0001, 0.005]
J120041	5.3±0.6 [‡]	6.2±0.6*	5.4±0.5	45.8	12	3.6	0.05	[3.1, 31]	[0.52, 10]	[0.001, 0.02]

Measured from an [†] unresolved, or [‡] barely resolved, **broad** component (see Fig. 7)

* Radial size limited by the GMOS-IFU Field-of-View

6.2 Outflow radius

Here we analyse the extent of the gas that couples with the outflows, separating it from an usually more extended one, that may include gas with ordered motion due to orbits in the galaxy potential, along with other kinematic deviations that can be associated with galaxy interactions.

We define the outflow radius as the extent of the region showing the broad component $R_{out} = R_b$. Table 3 displays their values, that reach up to ~ 2 –13 kpc, with an average of 6.6 ± 3.5 kpc. The largest extent is observed in J082313, and the smallest in J094521 that, as we suggested above, is not spatially resolved and probably has its outflow more directed towards the observer.

On the other hand, we associate the radial size measured from the *HST* [O III] images ($R_{[OIII]}$) with the Extended Narrow Line Region (ENLR, Unger et al. 1987), since it includes the contribution from all ionized gas, comprising all kinematic components. The same region is comprised by the extent of the full profile (R_{n+b}) measured in the IFS data, given that it contains not only the outflowing component, but also the remaining narrow ones. The $R_{[OIII]}$ values range between ~ 5 –26 kpc, while R_{n+b} varies between ~ 6 –18 kpc. However, the IFU FoV limits the extent of R_{n+b} in 6 QSOs of the sample (see Figs. 1). Therefore, in order to later compare the radial sizes of the outflow and the ENLR, we further define $R_{ENLR} = \max(R_{[OIII]}, R_{n+b})$, which results in values with an average of 13 ± 7 kpc.

Some previous studies on QSO 2’s extended gas emission report lower R_{out} values than ours. One reason for this discrepancy may be the different definitions for the outflow radii. While we identify it as corresponding to the maximum extent over which we observe the broadest component with S/N ratio in the flux $F_{[OIII],b} \geq 3$, Fischer et al. (2018), for example, considered the presence of an outflow only where there were components with peak velocities $|v_{[OIII]}| > 300 \text{ km s}^{-1}$, while Karouzos et al. (2016a) used a threshold for the presence of an outflow corresponding to $\sigma_{[OIII]} > \sigma_*$, where σ_* is the stellar velocity dispersion. These authors found values for the extent of the outflow below ~ 2 kpc.

Another issue is the beam-smearing due to the PSF of the observations (Husemann et al. 2016), that result in oversized extents when not corrected for it. To evaluate this effect, we first measured the FWHM/2 of the $F_{[OIII],b}$ radial profiles (FWHM_{out}/2) in Fig. 7. We then corrected it for the beam smearing using the approximation $\text{FWHM}_{out,0} = \sqrt{\text{FWHM}_{out}^2 - \text{FWHM}_{PSF}^2}$ (e.g. Tadhunter et al. 2018), that is valid for PSF and $F_{[OIII],b}$ distributions with 2D-Gaussian spacial profiles (which is not exactly true in both cases, but is an approximation). Finally, we corrected R_{out} adopting for it the same relation between the corrected and measured FWHM: $R_{out,0} = R_{out} \left(\frac{\text{FWHM}_{out,0}}{\text{FWHM}_{out}} \right)$. We did not attempt to propagate errors, since this method is highly uncertain. The new corrected values for the outflow radii $R_{out,0}$ range between ~ 1 –8 kpc, with an average of 4 ± 2 kpc, with the value of J094521 presented as an upper limit, as it is not resolved. We applied the same percentage correction to R_{n+b} , from which we have the new $R_{ENLR,0} = \max(R_{[OIII]}, R_{n+b,0})$. The corrected radial sizes are displayed in Table 4, along with the remaining corrected extents cited in this Section.

We can also compare our values with those obtained for similar objects by Villar-Martín et al. (2016), who adopted as the radius of the outflow half the FWHM of the flux distribution of the outflowing gas, obtaining values lower than 1–2 kpc after correcting for beam-smearing. In comparison, our FWHM_{out,0}/2 measurements returned values between ~ 0.5 –2.5 kpc, 4 ± 2 times lower than $R_{out,0}$, on average. The FWHM_{out,0}/2 extent can be viewed as a measure of the radial size of the bulk content of the outflow, while our $R_{out,0}$ measurement includes also the contribution of lower luminosity gas farther out. $R_{out,0}$ is thus expected to be larger than FWHM_{out,0}/2. Although we have tried to correct its value by the beam-smearing effect of the PSF, the method we have applied does not effectively remove its contribution to the wings of the spatial profile, which could result in an overestimation of $R_{out,0}$ in the less resolved cases (e.g. J085829; see Fig. 7).

Comparing the corrected outflow and ENLR extents, we obtained $R_{out,0}/R_{ENLR,0}$ values ranging between ~ 0.1 for J094521, and 0.9 for J12006, with an average of $\sim 0.5 \pm 0.3$. In

Table 4. PSF broadening correction. Sizes in units of kpc, where the subscript ‘0’ identifies the quantities for which the PFS correction was applied. (2) FWHM of the radial profile of the outflowing component; (3) Outflow extent; (4) ENLR extent; (5) Fraction of the radial extent affected by the outflow.

Name (1)	FWHM _{out,0} (2)	R _{out,0} (3)	R _{ENLR,0} (4)	R _{out,0} /R _{ENLR,0} (5)
J082313	2.3	7	26	0.3
J084135	2.3	5	9	0.6
J085829	2.6	5	7	0.7
J094521	1.2	< 1	13	0.1
J123006	3.6	8	9	0.9
J135251	3.2	4	19	0.2
J155019	4.8	5	7	0.7
J120041	0.94	3	5	0.6

comparison, Fischer et al. (2018) found a ~ 0.2 value for this ratio, with J120041, in particular, having $R_{out} = 1.07$ kpc, 3 times lower than our value. The smaller values of $R_{out,0}$ relative to $R_{ENLR,0}$ indicate that not all ionised gas is disturbed by the outflows. Therefore, it is essential to isolate the broad component, instead of simply using the extent of the total ionized gas as the outflow radius for obtaining the outflow properties.

6.3 Radial profiles of \dot{M}_{out} and \dot{E}_{out}

To explore the outflow strength, in Fig. 8 we plot the $\dot{M}_{out}(r)$ (left) and $\dot{E}_{out}(r)$ (right) radial profiles – with their maxima highlighted (stars) – calculated using the `default` assumptions.

The values of \dot{M}_{out} within 1 kpc (radial size not corrected for beam-smearing) from the nucleus range from ~ 0.1 to $10 M_{\odot} \text{ yr}^{-1}$, while the maximum values reach 3 to $30 M_{\odot} \text{ yr}^{-1}$ at radii of 1 to 5 kpc. The outflow powers range from 10^{40} to $10^{43} \text{ erg s}^{-1}$ within the inner kiloparsec, with maxima between $\sim 10^{41}$ and $10^{43} \text{ erg s}^{-1}$.

Since the PSF may affect the radial profiles of $\dot{M}_{out}(r)$ and $\dot{E}_{out}(r)$, we also plotted $\dot{E}_{out}(r)$ as function of the radius normalized by the σ_{PSF} in Fig. 9. For a better comparison between the profiles, we also normalized the $\dot{E}_{out}(r)$ values at $R = 2\sigma_{\text{PSF}}$. A comparison between these radial profiles shows that J084135 and J12004 seem to form a different group, with $\dot{M}_{out}(r)$ and $\dot{E}_{out}(r)$ peaking outside the nuclear region. Coincidentally J084135 is a clear major merger and J12004 has signs of a minor merger, and the velocities may be partly affected by the interactions. A similar trend – peak in the outflow away from the nucleus – has been observed by other authors in local Seyferts, although for much smaller scales (e.g. Crenshaw et al. 2015; Revalski et al. 2018b; Shimizu et al. 2019).

The other QSOs show a more continuous decay in the $\dot{E}_{out}(r)$ radial profiles, with J085829 and J094521 being the most compact, which could be caused by their unresolved broad component (Fig. 7), probably due to the fact that their outflow is more aligned with our LoS, as suggested by the dominance of negative values in the $v_{[\text{O III}]_b}$ maps (Figs. A3 and A4). In this scenario, the outflow axis of the two sources with $\dot{E}_{out}(r)$ peaking at the largest distances, J084135, J120041 and J082313, would be more perpendic-

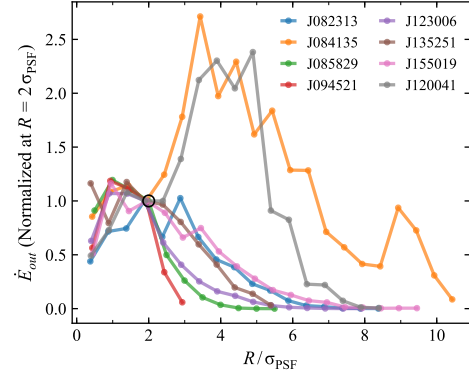


Figure 9. Same as the right panel of Fig. 8, but for the outflow power \dot{E}_{out} plotted as a function of the radius normalized by the PSF standard deviation: R/σ_{PSF} . The power is plotted in linear scale, and is normalized at $R = 2\sigma_{\text{PSF}}$ (black circle).

ular to the LoS. This hypothesis is reinforced by the mix of negative and positive values of $v_{[\text{O III}]_b}$ (Figs. A2 and A7) over the FoV, and the extended $[\text{O III}]$ emission. The remaining QSOs show $\dot{E}_{out}(r)$ radial profiles somewhat more extended than the two most compact ones.

6.4 Mass outflow rates and powers

In order to compare our data with previous results from the literature, in Fig. 10, we plot the maximum values of the $\dot{M}_{out}(r)$ and $\dot{E}_{out}(r)$ profiles as a function of L_{bol} , inspired by Figure 19 of Shimizu et al. (2019), and Fiore et al. (2017). Note that when referring to the peak values, we drop the ‘(r)’ \rightarrow for \dot{M}_{out} and \dot{E}_{out} . We list these values in Table 3, together with the kinetic coupling efficiencies $\epsilon_f = \dot{E}_{out}/L_{\text{bol}}$. We also list in this table the range of values obtained for these properties that result from tests we describe in the following Sections.

The blue stars in Fig. 10 correspond to the radial maxima obtained from the `default` assumptions: $\dot{M}_{out}^{\text{def}}$ and $\dot{E}_{out}^{\text{def}}$ (also shown as stars in the radial profile in Fig. 8). On average, the values are $\dot{M}_{out}^{\text{def}} = 10 \pm 8.8 M_{\odot} \text{ yr}^{-1}$ and $\dot{E}_{out}^{\text{def}} = (5.5 \pm 9.3) \times 10^{42} \text{ erg s}^{-1}$, with the corresponding kinetic coupling efficiencies ϵ_f^{def} ranging between 0.0007–0.4%. The blue bars refer to the range in the results obtained from assumptions distinct from the `default` ones (see Fig. 11), where we highlight with blue open stars, the values obtained when using the electron density traced by the $[\text{Ar IV}]$ emission-line ratio, what could be done only for two QSOs (see discussion in Section 4.2.1). With the exception of J094521, for which $\dot{M}_{out}^{\text{def}}$ and $\dot{E}_{out}^{\text{def}}$ fall on top of the $\epsilon_f = 0.5\%$ threshold, the others QSOs consistently fall below the Fiore et al. (2017) average powers for the same luminosities.

We note that the narrow3 component of J094521 shows only negative $v_{[\text{O III}]_n3}$ values, in the circumnuclear region, as well as high $\sigma_{[\text{O III}]_n3} > 300 \text{ km s}^{-1}$ in the nucleus and its Northwest (see Fig. A4), in the direction of the $[\text{O III}]$ blob seen in Fig. 1. J135251 also shows a similar disturbed region in the narrow2 (Fig. 6). These components may also be associated with outflows. Adding their contribution, the $\dot{M}_{out}^{\text{def}}$ and $\dot{E}_{out}^{\text{def}}$ values would increase by factors of $\sim 2-3$.

Table 5. Parameters of the tests. Each line shows the parameters used in each test, with the **default** ones listed in the first line. To be used together with Fig. 11; it shows the parameters used to obtain the \dot{M}_{out} and \dot{E}_{out} values listed in Tables 3, 6 and 7.

Test	Mass	Density	v_{out}	δr
default	$M_{H II b}$	$n_{e,[S II]_{n+b}}$	v_{95}	$\sigma_{PSF}/2$
integ.	$\sum M_{H II b}$	$\bar{n}_{e,[S II]_{n+b}}$	\bar{v}_{95}	R_b
n+b	$M_{H II n+b}$	-	-	-
v_{68}	-	-	v_{68}	-
proj	-	-	$v_{95,0}(i)$	$\sigma_{PSF}/2/\cos(i)$
$n_{e,BN19}$	-	$n_{e,BN19}$	-	-
$n_{e,[Ar IV]}$	-	$n_{e,[Ar IV]}$	-	-

However, in order to perform an homogeneous analysis for all objects, we keep using only the **broad** component in the **default** method.

We note that the assumptions made to obtain \dot{M}_{out} and \dot{E}_{out} in the different works included in Fig. 10 are not the same. Fiore et al. (2017) used homogeneous assumptions to redo the calculations from retrieved data of previous publications, using a constant low gas density of $n_e = 200 \text{ cm}^{-3}$, and an outflow velocity similar to ours v_{95} . Baron & Netzer (2019) calculated the electron density from the ionization parameter ($n_{e,BN19}$, see Section 4.2.1), with the R_{out} corresponding to the dust sublimation radius, whose temperature came from spectral energy distribution (SEDs) fitting. Trindade Falcão et al. (2020) used photoionization models to calculate the ionized gas mass and density, and deprojected their LoS velocity used in v_{out} , and – similarly to our work – used the peak values of the $\dot{M}_{out}(r)$ and $\dot{E}_{out}(r)$ radial profiles. These two latter works also obtained weaker outflow properties, compared to Fiore et al. (2017). On the other hand, Revalski et al. (2021) – also using photoionization models – found higher values, showing a similar trend compared to that of Fiore et al. (2017). We also added in Fig. 10 the low-luminosity AGNs data, compiled from the literature by Shimizu et al. (2019), corresponding to a variety of methods of calculation and resulting in large scattering of \dot{M}_{out} and \dot{E}_{out} values.

6.5 Influence of different calculation methods and assumptions on \dot{M}_{out} and \dot{E}_{out}

As already mentioned, the **default** method does not necessarily represent the best estimate for the feedback properties. It provides, however, an homogeneous method to be applied to all QSOs: ionized gas mass $M_{H II, b}$, calculated using only the outflowing component (**broad**); spatially resolved electron density $n_{e,[S II]_{n+b}}$, calculated from the [S II] line ratio (**narrow+broad**); and v_{95} as the outflow velocity. The radial profiles correspond to the mass outflow rates and powers crossing annuli with $\delta r = \sigma_{PSF}/2$ width, and therefore, does not assume that these rates are radially constant. From the peak of these curves, we obtained \dot{M}_{out}^{def} and \dot{E}_{out}^{def} .

Since different authors use different assumptions, and there is not a consensus about the best practice, in the following subsections we test how \dot{M}_{out} and \dot{E}_{out} are affected by different assumptions on: the ionized gas mass $M_{H II}$, the outflow velocity v_{out} , and the electron density n_e . In Table 5 we provide a quick reference to the parameters of the **default**

Table 6. Tests (part 1). Results of the tests with the **integrated** method (see also Table 5 and Section 6.5.1). (2) Mean of electron density obtained with [S II] (from the n+b component, in cm^{-3}); (3) Total ionized mass (from the b component, in M_\odot); (4) Mean of the v_{95} outflow velocity (in km s^{-1}); (5) Mass outflow rate (in $M_\odot \text{ yr}^{-1}$); (6) Outflow power (in $10^{42} \text{ erg s}^{-1}$). The values of the parameters (2)–(4) were calculated pixel-by-pixel, inside the outflow radius R_b .

Name	integrated ($\delta r = R_b$)				
	$\bar{n}_{e,[S II]_{n+b}}$	$\sum M_{H II, b}$	\bar{v}_{95}	\dot{M}_{out}^{int}	\dot{E}_{out}^{int}
(1)	(2)	(3)	(4)	(5)	(6)
J082313	290	2.3	540	0.97	0.091
J084135	120	1.4	710	1.7	0.27
J085829	340 [†]	2.5	1000	3.2	1.0
J094521	720 [†]	2.2	2000	22	29
J123006	370	1.2	980	0.98	0.41
J135251	260	1.6	1900	3.1	8.1
J155019	280	1.2	430	0.98	0.058
J120041	420	1.6	980	3.1	0.95

[†] Measured from the corresponding the SDSS spectrum

method, and what was changed in each test. Fig 11 visually shows how much the tests change the values of the **default** calculation of \dot{E}_{out} (the values are displayed in Tables 6 and 7). A version of the Fig. 11 for \dot{M}_{out} would be equal, except for the smaller relative variation due to the ‘ v_{68} ’ and ‘**proj**’ tests (discussed in Section 6.5.3), since $\dot{E}_{out}/\dot{M}_{out} \propto v_{out}^2$.

6.5.1 The integrated method (constant feedback rates)

We first tested the effect of using integrated and constant values within the outflow radius, which we have called the **integrated** method (Table 6). Here, we still applied Eqs. 1–3 but for $\delta r = R_b$ annular width, with the electron density and the outflow velocity becoming the average value within the whole region covered by outflow radius ($\bar{n}_{e,[S II]_{n+b}}$ and \bar{v}_{95}), while the ionized mass is summed over the same region ($\sum M_{H II, b}$). We still use only the flux from the **broad** component: $F_{H \alpha, b}$. Table 6 displays the values of these parameters, along with the resulting \dot{M}_{out}^{int} and \dot{E}_{out}^{int} .

Fig 11 doesn’t show a clear trend, with the majority of the QSOs lowering \dot{E}_{out}^{int} in comparison with its **default** value, and only two objects showing a increase, although small, resulting in a $\dot{E}_{out}^{int}/\dot{E}_{out}^{def}$ range of [1/4.5, 1.4]. Therefore, \dot{M}_{out} and \dot{E}_{out} values calculated with the **integrated** method are different from the peak of the corresponding radial profiles by a factor of ~ 3 on average, but are generally smaller.

6.5.2 Ionized gas mass (broad or narrow+broad)

The total flux from $H \alpha$ – here characterized by the **narrow+broad** components – includes not only the outflowing gas, but also gas in the galaxy and its vicinity (e.g. gas with ordered motion, spread by merges, etc). Hence, in order to calculate the mass outflow rates and powers it is important to include only the flux coming from the outflows – here traced by the **broad** component. This way we avoid overestimating the ionized gas mass, and subsequently, the mass outflow rate and its power, since both depend linearly on

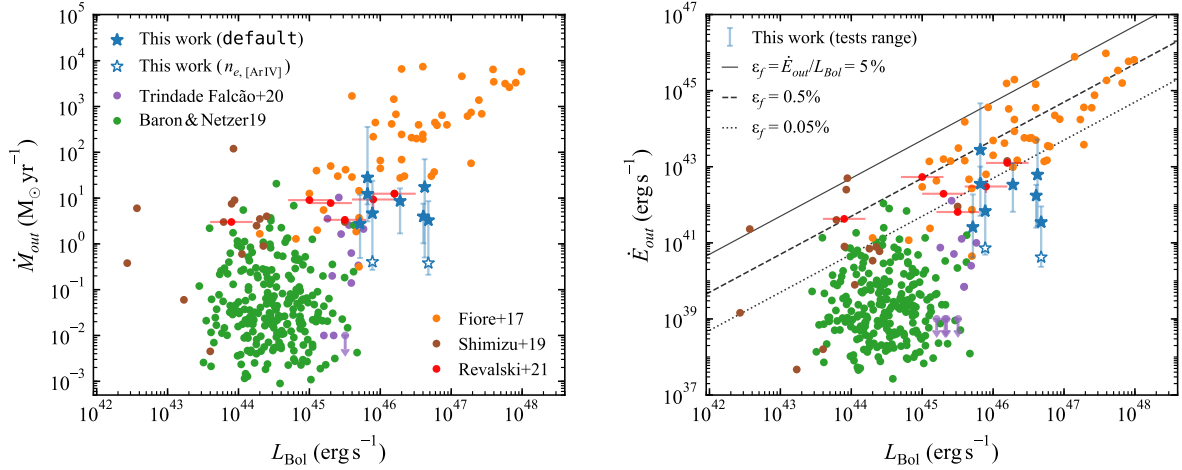


Figure 10. Mass outflow rate (\dot{M}_{out} , left) and outflow power (\dot{E}_{out} , right) as a function of the AGN bolometric luminosity (based on the similar figure of Shimizu et al. 2019). Our data, for the **default** assumptions, are presented as filled blue stars and the blue stars correspond to variations due to the tests listed in Fig. 11. For J082313 and J084135, we add blue stars corresponding to powers calculated using the gas density obtained from the [Ar IV] line ratio. We added the following data from the literature: orange circles, for the ionized outflows from Fiore et al. (2017); brown circles, for the data collected by Shimizu et al. (2019); purple circles, for Trindade Falcão et al. (2020); red errorbars, for Revalski et al. (2021); and green circles, for Baron & Netzer (2019). The dotted, dashed and solid black lines correspond to kinetic coupling efficiencies ϵ_f of 0.05%, 0.5% and 5%, respectively.

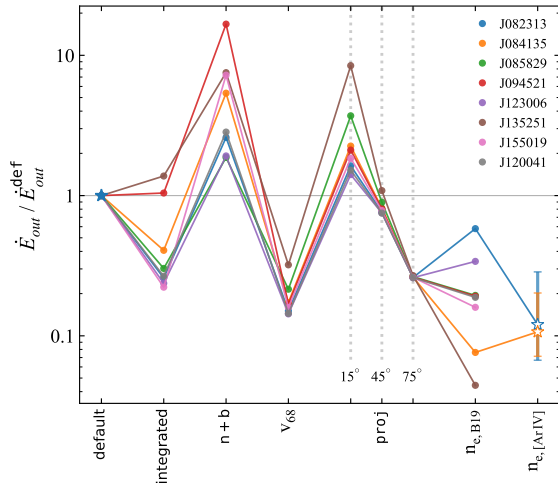


Figure 11. The effect of each test on the calculation of the outflow power (\dot{E}_{out}) in comparison to the **default** assumptions (See Section 6.5 for details, and Table 5 for a summary). **integrated**: method that assumes radially constant powers; **n+b**: uses the full extent of the H α emitting region (**narrow**+**broad**) to calculate M_{HII} (instead of only that of the **broad** component); **v₆₈**: outflow velocity as v_{68} instead of v_{95} ; **proj**: v_{out} and δr corrected for projection effects, for inclinations $i = 15, 45$ and 30° ; $n_{e, BN19}$: density from Baron & Netzer (2019, BN19) method (instead of $n_{e, [SII]}$); $n_{e, [ArIV]}$: density from the [Ar IV] emission line ratio.

M_{HII} . In order to quantify the effect of including also the mass of the narrow components in the calculations, we recalculate the feedback properties, using the total ionized gas mass (from $F_{H\alpha, n+b}$) instead of only the outflowing one (from $F_{H\alpha, b}$). These values are displayed in Table 7.

Fig 11 shows that the results lead to an increase in $\dot{E}_{out}^{n+b} / \dot{E}_{out}^{def}$, with the values ranging between [1.9, 17]. Therefore, without isolating the contribution from the outflows in the total flux observed, the powers can be overestimated up to one order of magnitude.

Some authors, instead of decomposing the emission-line profiles into multiple Gaussians, estimate the outflowing gas mass from the percentage of the emission-line flux that has velocities above certain threshold. For example, Ruschel-Dutra et al. (submitted); Sun et al. (2017); Kakkad et al. (2020) used a threshold of $w_{80} > 600 \text{ km s}^{-1}$ as the minimum value to consider the gas to be in outflow, where w_{80} is the width of an emission line profile above which 80% of the total flux is emitted. This condition helps to avoid false outflow identifications, including only the the highest gas velocities that cannot be in mere orbital motion. On the other hand, a spectrum with multiple narrow components – that could be related with mergers – will also result in a larger w_{80} . For example, our J084135 spectra – without considering the **broad** component – have three **narrow** components (see Fig. 3), that would increase the value of w_{80} if this method would be applied here. Other issue is that this condition does not include the contribution of less powerful winds.

The discussion above highlights the importance of accessing how much does the outflowing component contributes to the measured flux. This can be best done with IFS (e.g. Gallagher et al. 2019), or imaging + long-slit observations (e.g. Trindade Falcão et al. 2020). Without resolved spectroscopy, the calculation can be improved by using profile decomposition – as done here – to measure the contribution of the outflows in a single spectrum (e.g. Rose et al. 2018; Baron & Netzer 2019).

Table 7. Tests (part 2): Results of the tests about effect of the mass, the outflow velocity and the electron density in the calculations of the feedback properties (see also Table 5 and Sections 6.5.2–6.5.5). Mass outflow rates (\dot{M}_{out}) in units of $M_{\odot} \text{ yr}^{-1}$, and outflow powers (\dot{E}_{out}) in units of $10^{42} \text{ erg s}^{-1}$. (1) Galaxy short name; (2)–(3) Results of using the full profile (n+b) of H α to calculate $M_{\text{H II}}$, instead of only the b component; (4)–(5) v_{68} as outflow velocity, instead of v_{95} ; (6)–(7) outflow velocity corrected for inclinations $i=45 \pm 30^{\circ}$; (8) average of the density calculated with the [Baron & Netzer \(2019, BN19\)](#) method (not used to calculate $\dot{E}_{out}^{\text{BN19}}$ and $\dot{E}_{out}^{\text{BN19}}$); (9)–(10) Results of using $n_{e,\text{BN19}}$ with radial dependence (see Fig. 5) to obtain $M_{\text{H II}}$, \dot{E}_{out} and \dot{E}_{out} ; (11) density calculated from the [Ar IV] lines ratios; (12)–(13) Results of using $n_{e,[\text{Ar IV}]}$.

Name (1)	Ionized Mass		Outflow velocity				Electron density					
	\dot{M}_{out}^{n+b} (2)	\dot{E}_{out}^{n+b} (3)	\dot{M}_{out}^{v68} (4)	\dot{E}_{out}^{v68} (5)	$\dot{M}_{out}^{\text{proj}}$ (6)	$\dot{E}_{out}^{\text{proj}}$ (7)	$\bar{n}_{e,\text{BN19}}$ (8)	$\dot{M}_{out}^{\text{BN19}}$ (9)	$\dot{E}_{out}^{\text{BN19}}$ (10)	$n_{e,[\text{Ar IV}]}$ (11)	$\dot{M}_{out}^{[\text{Ar IV}]}$ (12)	$\dot{E}_{out}^{[\text{Ar IV}]}$ (13)
J082313	8.6	0.91	1.8	0.053	$2.4_{1.4}^{4.5}$	$0.27_{0.18}^{0.3}$	370	2.1	0.2	1450_{840}^{1150}	$0.38_{0.17}^{0.53}$	$0.04_{0.019}^{0.058}$
J084135	24	3.7	2.6	0.12	$3.4_{2.2}^{4.2}$	$0.56_{0.38}^{0.99}$	1300	0.65	0.052	870_{410}^{430}	$0.41_{0.13}^{0.36}$	$0.07_{0.024}^{0.065}$
J085829	16	6.3	5.2	0.73	$6.6_{4.3}^{6.4}$	$3_{2.1}^{9.5}$	1100	1.7	0.66	-	-	-
J094521	360	460	16	4.7	21_{13}^{15}	22_{15}^{36}	3800	15	5.3	-	-	-
J123006	7.6	3.3	2.1	0.25	$2.9_{1.8}^{1.5}$	$1.3_{0.86}^{1.2}$	740	0.49	0.041	-	-	-
J135251	71	46	12	2	$14_{9.7}^{22}$	6.7_5^{45}	10000	3.2	0.67	-	-	-
J155019	12	1.9	1.5	0.041	$2_{1.3}^{1.4}$	$0.2_{0.14}^{0.28}$	1700	0.49	0.041	-	-	-
J120041	31	10	6.5	0.51	$8.9_{5.7}^{4.7}$	$2.7_{1.7}^{2.7}$	1100	3.2	0.67	-	-	-

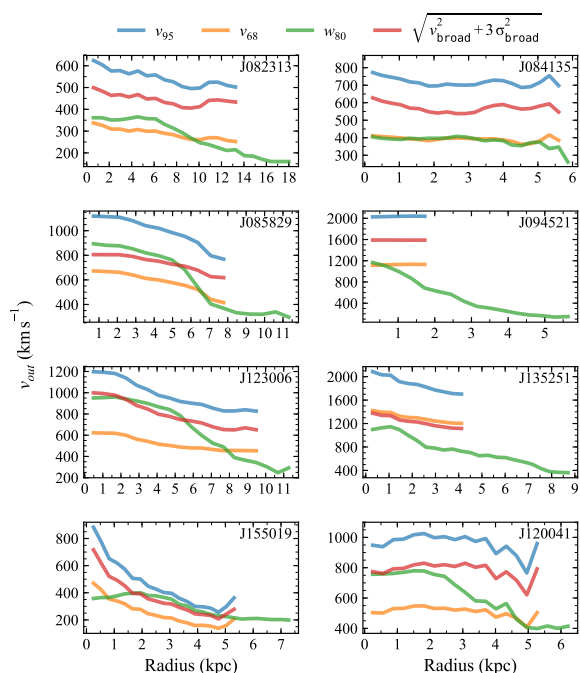


Figure 12. Radial profiles of different definitions for the outflow velocity v_{out} for each QSO of the sample: v_{95} in blue, v_{68} in orange, w_{80} in green and $\sqrt{v_{\text{broad}}^2 + 3\sigma_{\text{broad}}^2}$ in red (Section 6.5.3).

6.5.3 Outflow velocity

Another issue concerning feedback properties of outflows is what velocity should be used to characterize the outflow. In this work, we used $v_{95} = |v_{\text{broad}}| + 2\sigma_{\text{broad}}$, where σ_{broad} and v_{broad} are the velocity dispersion of the broad component, and its velocity shift from the systemic velocity, respectively, measured from [O III]. This parametrization weights the con-

tribution of the highest velocities in the outflow, using a value close to its maximum (e.g. [Rupke & Veilleux 2013](#); [Fiore et al. 2017](#)). Therefore, since $\dot{M}_{out} \propto v_{out}$ and $\dot{E}_{out} \propto v_{out}^3$, using v_{95} as the outflow velocity results in higher values of mass outflow rates and powers when compared with other v_{out} definitions. To check this, we tested the effect of using another parametrization $v_{68} = |v_{\text{broad}}| + \sigma_{\text{broad}}$. This definition returns smaller values, as shown in Fig. 12, where we compare the radial velocity profiles of v_{95} and v_{68} , along with other two v_{out} parametrizations, that are discussed later in this Section.

As expected, Fig 11 shows that this test decreases the values of the powers, with $\dot{E}_{out}^{v68}/\dot{E}_{out}^{\text{def}}$ ranging between [1/7.1, 1/3.1], an average of ~ 5 times lower than the default assumptions, while \dot{M}_{out}^{v68} decreased by a factor of ~ 2 .

Several other parametrizations for v_{out} have been used in the literature, such as $\sqrt{v_{\text{broad}}^2 + \sigma_{\text{broad}}^2}$ (e.g. [Karouzos et al. 2016a](#); [Baron & Netzer 2019](#)) and $|v_{\text{broad}}| + \text{FWHM}/2$ (e.g. [Bischetti et al. 2019](#); [Gallagher et al. 2019](#)). Another approach is to use non-parametric definitions, that have the advantage of being non-dependent of a rigorous emission line fit, which is a source of error in our measurements. One of the most used is w_{80} (e.g. [Liu et al. 2013b](#); [Sun et al. 2017](#)). Comparing its radial profile with those of v_{95} and v_{68} in Fig. 12, the first noticeable feature is that the w_{80} profiles are the most extended. This happens because w_{80} – differently from the other definitions – is not limited by the S/N of the broad component, but by S/N of the full [O III] profile (narrow+broad). Differently from [Fiore et al. \(2017\)](#), that argued that w_{80} is close to v_{95} , we found that this happens only in the outer parts of the J155019’s emitting region, being lower in the other regions in this object, and also for the remaining QSOs. Besides, w_{80} is close to or smaller than v_{68} in four other QSOs, and stays between v_{68} and v_{95} in the remaining three: there isn’t a clear pattern, other than $w_{80} < v_{95}$, in general.

We note also that sometimes the velocity dispersion

of the outflowing gas is included in the evaluation of outflow power: $\dot{E}_{out} = \dot{M}_{out} (v_{out}^2 + 3\sigma_{out}^2)/2$ (e.g. Harrison et al. 2018; Rose et al. 2018). If we use $v_{out} = v_{broad}$ and $\sigma_{out} = \sigma_{broad}$ in this formula, it will be equivalent to use $v_{out} = \sqrt{v_{broad}^2 + 3\sigma_{broad}^2}$ in our Eq. 4. In this case, Fig. 12 shows that the results would be between our previous ones for v_{95} and v_{68} , except for J135251, which closely follows v_{68} .

6.5.4 Projection effects

Projection effects due to the outflows inclinations (i) – angle between the outflow axis and the plane of the sky – will affect the velocity and distance measurements. We tested this effect by calculating deprojected velocities (v_0) and annular widths (Δx_0) as: $v_0 = v_{obs}/\sin(i)$ and $\Delta x_0 = \Delta x_{obs}/\cos(i)$, where v_{obs} and Δx_{obs} are the observed values. Applying these corrections for $v_{out,0} = v_{95,0} = (|v_{broad}|/\sin(i) + 2\sigma_{broad})$ and $\delta r_0 = \delta r/\cos(i)$, we recalculated \dot{M}_{out} and \dot{E}_{out} , for $i = 15, 45$ and 75° .

Fig. 11 displays the results for each of the inclinations above. On average, $\dot{E}_{out}^{proj}/\dot{E}_{out}^{def}$ decreases by a factor of ~ 4 for $i = 75^\circ$ (range of [1/3.8, 1/3.7]), and increases by a average factor of ~ 3 for $i = 15^\circ$ (range of [1.4, 8.4]), with small changes for $i = 45^\circ$ (range of [1/1.3, 1.1]).

Ignoring the σ_{broad} term in $v_{out,0}$, this variation comes from the definitions used in Eqs. 3 and 4: $\dot{M}_{out}^{proj} \propto v_{out}/\delta r \propto [\cos(i)/\sin(i)]$ and $\dot{E}_{out}^{proj} \propto v_{out}^3/\delta r \propto [\cos(i)/\sin^3(i)]$. Consequently, \dot{M}_{out}^{proj} decreases for $i > 45^\circ$ and increases for lower inclinations, while for \dot{E}_{out} , the ‘turning point’ occurs at $i \sim 55^\circ$. Therefore, since we did not apply these corrections to the **default** method, the obtained values correspond to inclinations of $i \sim 50^\circ$.

We conclude that the projection effects are a important source of uncertainty, inducing changes in $\dot{E}_{out}^{proj}/\dot{E}_{out}^{def}$ between [1/3.8, 8.4], for $i = 75^\circ$ and 15° , and even higher for inclinations outside this range.

6.5.5 Electron density

Recent studies have been pointing out problems with the use of the [S II] $\lambda\lambda 6718,31$ ratio to obtain the density of the ionized gas in outflow (Harrison et al. 2018; Davies et al. 2020), suggesting that this density estimator results in smaller values of n_e than those representative of these regions. Rose et al. (2018), using the auroral [O II] $\lambda\lambda 7319,31$ lines and the trans-auroral lines of [S II] $\lambda\lambda 4068,76$ (method introduced by Holt et al. 2011), found densities between $10^{3.4} - 10^{4.8} \text{ cm}^{-3}$, one to two orders of magnitude higher than the values obtained from [S II] $\lambda\lambda 6718,31$. Baron & Netzer (2019) presented another method, based on the ionization parameter U , obtaining even higher values for some objects, with n_e ranging between $\sim 10^3 - 10^6 \text{ cm}^{-3}$.

A value of the electron density representative of the outflows is important for the calculation of the mass outflow rates and powers since the ionized gas mass is inversely proportional to n_e , and consequently, $\dot{M}_{out} \cdot \dot{E}_{out} \propto 1/n_e$. Therefore, we tested other density estimators, starting with the method introduced by Baron & Netzer (2019) to obtain $n_{e,BN19}$. Figure 5 displays the radial profiles of $n_{e,BN19}$ as black dotted bars for annuli with a width corresponding to FWHM_{PSF} . In this method the density is highly dependent on

the outflow radius, with $n_{e,BN19} \propto 1/r^2$, as seen in the radial profiles decay. For reference, in Table 7 we present the average density values $\bar{n}_{e,BN19}$ along each radial profile, with an average among all QSOs of 2500 cm^{-3} and high standard deviation of 3500 cm^{-3} . In comparison, the $n_{e,[S II]n+b}$ average value is only $350 \pm 170 \text{ cm}^{-3}$ (Table 6). Individually, J082313 and J120041 present $n_{e,BN19}(r)$ radial profiles values similar to those calculated from [S II]. Davies et al. (2020) obtained similar results by also testing different methods for calculating n_e : an average of 1900 cm^{-3} with the Baron & Netzer (2019) method, 4800 cm^{-3} from the trans-auroral/auroral lines, and only 350 cm^{-3} from the [S II] ratio.

Using the radial profiles of $n_{e,BN19}$, we obtained $\dot{E}_{out}^{BN19}/\dot{E}_{out}^{def}$ in the range [1/42, 1/1.7], with values ~ 5 times lower on average than the **default** values, as shown in Fig. 11. This is expected because $n_{e,BN19} > n_{e,[S II]n+b}$, with the large variance in $\dot{E}_{out}^{BN19}/\dot{E}_{out}^{def}$ reflecting the large range of $n_{e,BN19}$ values among the sample. In particular, for J120041, Trindade Falcão et al. (2020) obtained the density from a photoionization model with a constant ionization parameter, resulting in lower peak values than \dot{M}_{out}^{BN19} and \dot{E}_{out}^{BN19} by factors of ~ 1.5 and 7 , respectively. In part, the difference arises from the smaller $v_{out} = |v_b|$ definition used by these authors, which affects more the \dot{E}_{out} values.

One of the issues with the traditional [S II] method is that the [S II] $\lambda\lambda 6718,31$ ratio is sensitive to n_e in the range of $50 - 5000 \text{ cm}^{-3}$ (Harrison et al. 2018), with high uncertainties at the extreme values. Another problem is that the ionization potential of S I \rightarrow S II (10.36 eV) is much lower than that of O II \rightarrow O III (35.1 eV) (Proxauf et al. 2014), whose emission lines are the usual tracers of the gas in outflow, as we have used here (the profile is dominated by more perturbed kinematics than most of the other emission lines). This difference in the ionization potential, plus the difference in critical densities, indicates that the [S II] and [O III] emission may originate in different regions within the galaxies. A possible solution is to use [Ar IV] $\lambda\lambda 4011,40$ emission lines – that have an ionization potential Ar III \rightarrow Ar IV of 40.7 eV (Proxauf et al. 2014). However, its usual small S/N ratio is an obstacle. Only two of our objects – J082313 and J084135 – have their integrated spectrum with S/N > 3 for these lines. The corresponding values of $n_{e,[Ar IV]}$ are 1450_{840}^{1150} and $870_{410}^{430} \text{ cm}^{-3}$, respectively. Comparing with the average values obtained from the [S II] ratio (see Fig. 5), we see that both are higher, with $n_{e,[Ar IV]}/\bar{n}_{e,[S II]n+b} \sim 5 \pm 4$ and 7 ± 4 , respectively.

Once more, the corresponding powers decrease (Fig. 11), with $\dot{E}_{out}^{[Ar IV]}/\dot{E}_{out}^{def}$ values of $0.12_{0.22}^{0.17}$ for J082313 and $0.11_{0.26}^{0.19}$ for J084135, ~ 9 times lower, on average. We highlighted the new values in Fig. 10, to show that better density calculations lead to values below the reference AGN coupling efficiencies (discussed in the next Section).

The [Ar IV] lines are not commonly used in the literature to obtain gas densities for AGN-like objects. Two recent papers have used them: May et al. (2018) found $n_{e,[Ar IV]} \sim 10^{3.6} \text{ cm}^{-3}$ for Low-luminosity AGN; Cerqueira-Campos et al. (2021) used them for three Coronal-Line Forest AGN (CLiF AGN), finding a range of $\sim 10^{3.4} - 10^{4.2} \text{ cm}^{-3}$, with $n_{e,[Ar IV]}/n_{e,[S II]} \sim 5 - 17$ (in agreement with to our values). The main reason for these lines not to be used frequently seems to be the weak intensity of [Ar IV]: for the

two QSOs for which we could measure them – J082313 and J084135 – the ratio $F_{[\text{O III}]\lambda 5007}/F_{[\text{Ar IV}]\lambda 4011}$ are ~ 450 and 380 , respectively.

Another source of uncertainty in our analysis comes from the determination of the bolometric luminosities (L_{bol}), which were obtained from the total $[\text{O III}]\lambda 5007$ luminosity (Trump et al. 2015). Dust extinction is an issue in this method (Heckman & Best 2014), although we followed the Lamastra et al. (2009) prescription for correcting it for reddening. Errors in L_{bol} affect the results displayed in Fig. 10, since, for example, lower values would bring our points closer to the $\epsilon_f = 0.5\%$ line. More importantly, it introduces uncertainties in the measurement of ϵ_f . We note that there are still further sources of uncertainties that were not taken into account, such as those due to reddening, density gradients, and geometry.

6.5.6 AGN coupling efficiency

In studies about the impact of AGNs on their host galaxies, the AGN coupling efficiency – the percentage of the L_{bol} that couples with the ISM – is often calculated, since it has been suggested that its value may define if the feedback is powerful enough to affect the evolution of the host galaxy. Using simulations of galaxy mergers as triggers of AGNs, Di Matteo et al. (2005) found that a value of $5\%L_{\text{bol}}$ reproduces the $M_{\text{BH}} - \sigma_*$ relation. However, assuming that the feedback only needs to drive winds on the hot gas, that subsequently propagates to the cold part, Hopkins & Elvis (2010) found a threshold coupling efficiency of 0.5% , an order of magnitude lower. Zubovas (2018) obtain similar values for higher redshift ($z \sim 3$) AGN, but higher at low redshifts, of 13% at $z \sim 0.5$. In hydrodynamical simulations, for example, Schaye et al. (2015) used $20\%L_{\text{bol}}$, while Nelson et al. (2019) used 15% for the radiative-mode feedback, both injecting the energy thermally into the ISM. In this work, we provide the kinetic coupling efficiency $\epsilon_f = \dot{E}_{\text{out}}/L_{\text{bol}}$ for the ionized gas, since \dot{E}_{out} as we have calculated measures only this kinetic component.

Using the `default` assumptions, the kinetic coupling efficiencies ϵ_f^{def} vary from 0.0007% for J082313, to 0.4% for J094521. Only the latter shows a value of ϵ_f^{def} close to the above threshold from Hopkins & Elvis (2010), with the remaining QSOs showing values below $\epsilon_f = 0.05\%$. The average and median values are 0.6 and 0.1% , respectively. However, our tests show that these measurements are highly uncertain. Putting together all tests results, ϵ_f ranges between 0.00005 and 7% . In particular, the densities obtained with $[\text{S II}]$ in the `default` method are not ideal. The possibly more adequate values, calculated from the $[\text{Ar IV}]$ emission line ratio, lead to an order of magnitude decrease in the efficiencies.

Our values of ϵ_f and the uncertainties involved in the quantities inferred from the observations support the results from many recent studies (e.g. Karouzos et al. 2016b; Villar Martín et al. 2014; Villar-Martín et al. 2016; Fischer et al. 2018; Husemann et al. 2016; Spence et al. 2018; Rose et al. 2018). However, a direct comparison between our kinetic coupling efficiencies, and the ones obtained in models and simulations, cannot be made. As pointed out previously by Harrison et al. (2018), ϵ_f as we have calculated determines the coupling efficiency only of the kinetic component ob-

tained from the ionized gas, while values provided by models and used in simulations usually refer to the total energy deposited in ISM, where only a fraction may actually induce outflows observed in ionized gas. For example, part of the energy is used to heat and ionize the gas (Zubovas 2018). Even more important is the fact that the we are measuring only a fraction of the gas affected by the feedback – the ionized phase. Fiore et al. (2017) found that molecular winds contribute more to the energy released in the AGN feedback than the ionized gas, although ionized gas outflows increase their impact for higher L_{bol} sources. Other important phases that should be considered include the neutral (e.g. $\text{H I } 21\text{cm}$, Na I D , C II) and the highly ionized (X-ray absorption lines) (Cicone et al. 2018; Harrison et al. 2018; Fiore et al. 2017). Hence, these effects may explain our lower coupling efficiencies in comparison to those predicted by models.

7 CONCLUSIONS

We have analysed optical integral field spectroscopy data of a sample of 8 QSO 2's at $0.1 \leq z \leq 0.5$ in order to map the ionized gas kinematics and quantify mass outflow rates and powers from their AGN. The main conclusions of this paper are:

- Most of the emission-line profiles were best fitted by one or two narrow components – attributed to ambient gas, and sometimes associated with mergers – plus a broader one (broad) – attributed to a nuclear outflow;

While the total ionized gas emission extents reach distances from the nucleus of $5 \lesssim R_{\text{ELNR},0} \lesssim 26$ kpc, the outflows show smaller extents in the range $1 \lesssim R_{\text{out},0} \lesssim 8$ kpc. Therefore, only part of the ionised gas is disturbed by the outflows, with an average ratio of $R_{\text{out}}/R_{\text{ENLR}} \sim 0.5 \pm 0.3$.

- We have measured the mass outflow rates (\dot{M}_{out}) and powers (\dot{E}_{out}) from the kinematics of the broader component as a function of distance from the nucleus. These measurements were first made using the `default` assumptions: gas density determined from the $[\text{S II}]$ line ratio, outflow velocity as v_{95} , and the gas mass from the luminosity of the broad component only. With these assumptions, we found peak values of $\dot{M}_{\text{out}}^{\text{def}}$ ranging between $\sim 3 - 30 M_{\odot} \text{ yr}^{-1}$, and peak outflow powers $\dot{E}_{\text{out}}^{\text{def}}$ values between $\sim 3 \times 10^{41} - 3 \times 10^{43} \text{ erg s}^{-1}$.

- We performed tests to check the influence in the resulting \dot{M}_{out} and \dot{E}_{out} of varying assumptions regarding: the ionized gas mass, the outflow velocity, the ionized gas density and orientation of the outflow. When compared with the `default` method, these tests resulted in typical variations of one order of magnitude for each test, and being larger if considered together.

- Including the total ionized gas mass in the calculations (instead of only the contribution from the broad component) lead to overestimates of the outflow powers by factors of $\sim 2 - 17$. Values based on integrated measurements – as in unresolved observations – differ from the peak of radial profile values by factors of up to ~ 5 .

- The use of lower outflow velocities (v_{out}) than the `default` v_{95} lead to a decrease of ~ 5 times in \dot{E}_{out} , and ~ 2 times in \dot{M}_{out} , on average. Corrections for projection effects also change \dot{E}_{out} , decreasing it – on average – by a factor of ~ 4 for inclinations $i = 75^\circ$, and increasing it by a factor of ~ 2 for $i = 15^\circ$.

- The use of improved density tracers instead of the [S II] ratio, resulted in higher density values, with an average increase of $n_{e,\text{BN19}}/\bar{n}_{e,[\text{S II}]} \sim 7$ (with high variations) for the method based on the ionization parameter, and an increase of $\bar{n}_{e,[\text{Ar IV}]}/\bar{n}_{e,[\text{S II}]} \sim 6 \pm 3$ for values obtained from the [Ar IV] ratio. The resulting outflow powers decrease by the same factors. We recommend the use of [Ar IV], since its ionization potential is similar to the [O III] one;

- From the peak values of $\dot{E}_{out}^{\text{def}}$, we calculated the corresponding kinetic coupling efficiencies ϵ_f^{def} , finding values in the range $7 \times 10^{-4} - 0.05\%$, except for J094521, that has $\epsilon_f^{\text{def}} \sim 0.4\%$. Including the results from the tests, the range becomes $5 \times 10^{-5} - 7\%$. In particular, using the densities calculated from the [Ar IV] tracer, we observe almost one order of magnitude decrease in the coupling efficiencies.

We finally point out that the **default** assumptions used in this study do not necessarily represent the best choice of parameters, but are useful as a reference baseline for the tests. We also remind the reader that, since this work only refers to the kinetic feedback from the ionized gas, it underestimates the actual fraction of the bolometric luminosity that couples with the ISM, as contributions of feedback from other gas phases, such as the molecular gas and hotter X-ray emitting gas should also be considered, as well as other forms of feedback.

ACKNOWLEDGEMENTS

This study was financed in part by the Coordenação de Aperfeiçoamento de Pessoal de Nível Superior (CAPES-Brasil, 88887.478902/2020-00) and Conselho Nacional de Desenvolvimento Científico e Tecnológico (CNPq-Brasil, 130574/2018-0).

DATA AVAILABILITY

Based on observations obtained at the international Gemini Observatory, a program of NSF’s NOIRLab, and available from Gemini Observatory Archive (program ID in Table 2), which is managed by the Association of Universities for Research in Astronomy (AURA) under a cooperative agreement with the National Science Foundation. on behalf of the Gemini Observatory partnership: the National Science Foundation (United States), National Research Council (Canada), Agencia Nacional de Investigación y Desarrollo (Chile), Ministerio de Ciencia, Tecnología e Innovación (Argentina), Ministério da Ciência, Tecnologia, Inovações e Comunicações (Brazil), and Korea Astronomy and Space Science Institute (Republic of Korea).

REFERENCES

Allington-Smith J., et al., 2002, *PASP*, **114**, 892
 Bae H.-J., Woo J.-H., 2016, *ApJ*, **828**, 97
 Baldwin J. A., Phillips M. M., Terlevich R., 1981, *PASP*, **93**, 5
 Baron D., Netzer H., 2019, *MNRAS*, **486**, 4290
 Bellocchi E., Arribas S., Colina L., Miralles-Caballero D., 2013, *A&A*, **557**, A59

Bischetti M., Maiolino R., Carniani S., Fiore F., Piconcelli E., Fluitsch A., 2019, *A&A*, **630**, A59
 Blanton M. R., et al., 2017, *AJ*, **154**, 28
 Cerqueira-Campos F. C., Rodríguez-Ardila A., Riffel R., Marinello M., Prieto A., Dahmer-Hahn L. G., 2021, *MNRAS*, **500**, 2666
 Chen X., Akiyama M., Noda H., Abdurro’uf Toba Y., Yamamura I., Kawaguchi T., Kokubo M., Ichikawa K., 2019, *PASJ*, **71**, 29
 Cicone C., et al., 2014, *A&A*, **562**, A21
 Cicone C., et al., 2015, *A&A*, **574**, A14
 Cicone C., Brusa M., Ramos Almeida C., Cresci G., Husemann B., Mainieri V., 2018, *Nature Astronomy*, **2**, 176
 Couto G. S., Storchi-Bergmann T., Siemiginowska A., Riffel R. A., Morganti R., 2020, *MNRAS*, **497**, 5103
 Crenshaw D. M., Kraemer S. B., 2007, *ApJ*, **659**, 250
 Crenshaw D. M., Fischer T. C., Kraemer S. B., Schmitt H. R., 2015, *ApJ*, **799**, 83
 Cresci G., et al., 2015, *ApJ*, **799**, 82
 Croton D. J., et al., 2016, *ApJS*, **222**, 22
 Davies R., et al., 2020, *MNRAS*, **498**, 4150
 Di Matteo T., Springel V., Hernquist L., 2005, *Nature*, **433**, 604
 Fabian A. C., 2012, *ARA&A*, **50**, 455
 Ferrarese L., Merritt D., 2000, *ApJ*, **539**, L9
 Feruglio C., et al., 2015, *A&A*, **583**, A99
 Fiore F., et al., 2017, *A&A*, **601**, A143
 Fischer T. C., Crenshaw D. M., Kraemer S. B., Schmitt H. R., 2013, *ApJS*, **209**, 1
 Fischer T. C., et al., 2018, *ApJ*, **856**, 102
 Fixsen D. J., Cheng E. S., Gales J. M., Mather J. C., Shafer R. A., Wright E. L., 1996, *ApJ*, **473**, 576
 Gallagher R., Maiolino R., Belfiore F., Drory N., Riffel R., Riffel R. A., 2019, *MNRAS*, **485**, 3409
 Gebhardt K., et al., 2000, *ApJ*, **539**, L13
 Gonzalez-Perez V., Lacey C. G., Baugh C. M., Lagos C. D. P., Helly J., Campbell D. J. R., Mitchell P. D., 2014, *MNRAS*, **439**, 264
 Halpern J. P., Steiner J. E., 1983, *ApJ*, **269**, L37
 Harrison C. M., Alexander D. M., Mullaney J. R., Swinbank A. M., 2014, *MNRAS*, **441**, 3306
 Harrison C. M., Costa T., Tadhunter C. N., Fluitsch A., Kakkad D., Perna M., Vietri G., 2018, *Nature Astronomy*, **2**, 198
 Heckman T. M., Best P. N., 2014, *ARA&A*, **52**, 589
 Holt J., Tadhunter C. N., Morganti R., Emonts B. H. C., 2011, *MNRAS*, **410**, 1527
 Hopkins P. F., Elvis M., 2010, *MNRAS*, **401**, 7
 Husemann B., Scharwächter J., Bennert V. N., Mainieri V., Woo J. H., Kakkad D., 2016, *A&A*, **594**, A44
 Jarvis M. E., et al., 2019, *MNRAS*, **485**, 2710
 Kakkad D., et al., 2020, *A&A*, **642**, A147
 Karouzos M., Woo J.-H., Bae H.-J., 2016a, *ApJ*, **819**, 148
 Karouzos M., Woo J.-H., Bae H.-J., 2016b, *ApJ*, **833**, 171
 Lamastra A., Bianchi S., Matt G., Perola G. C., Barcons X., Carrera F. J., 2009, *A&A*, **504**, 73
 Liu G., Zakamska N. L., Greene J. E., Nesvadba N. P. H., Liu X., 2013a, *MNRAS*, **430**, 2327
 Liu G., Zakamska N. L., Greene J. E., Nesvadba N. P. H., Liu X., 2013b, *MNRAS*, **436**, 2576
 Maiolino R., et al., 2012, *MNRAS*, **425**, L66
 May D., Rodríguez-Ardila A., Prieto M. A., Fernández-Ontiveros J. A., Diaz Y., Mazzalay X., 2018, *MNRAS*, **481**, L105
 Naab T., Ostriker J. P., 2017, *ARA&A*, **55**, 59
 Nelson D., et al., 2019, *MNRAS*, **490**, 3234
 Novak M., et al., 2020, arXiv e-prints, p. arXiv:2010.14875
 Osterbrock D. E., Ferland G. J., 2006, *Astrophysics of gaseous nebulae and active galactic nuclei*, 2 edn. University Science Books, Sausalito, CA
 Proxauf B., Öttl S., Kimeswenger S., 2014, *A&A*, **561**, A10

Ramos Almeida C., Piqueras López J., Villar-Martín M., Bessiere P. S., 2017, *MNRAS*, **470**, 964

Revalski M., Crenshaw D. M., Kraemer S. B., Fischer T. C., Schmitt H. R., Machuca C., 2018a, *ApJ*, **856**, 46

Revalski M., et al., 2018b, *ApJ*, **867**, 88

Revalski M., et al., 2021, arXiv e-prints, p. arXiv:2101.06270

Reyes R., et al., 2008, *AJ*, **136**, 2373

Riffel R. A., Storch-Bergmann T., Winge C., 2013, *MNRAS*, **430**, 2249

Riffel R. A., Storch-Bergmann T., Zakamska N. L., Riffel R., 2020, *MNRAS*, **496**, 4857

Rose M., Tadhunter C., Ramos Almeida C., Rodríguez Zaurín J., Santoro F., Spence R., 2018, *MNRAS*, **474**, 128

Rupke D. S. N., Veilleux S., 2013, *ApJ*, **768**, 75

Ruschel-Dutra D., 2020, danielrd6/ifscube v1.0, doi:10.5281/zenodo.3945237, https://doi.org/10.5281/zenodo.3945237

Savage B. D., Mathis J. S., 1979, *ARA&A*, **17**, 73

Schaye J., et al., 2015, *MNRAS*, **446**, 521

Seaton M. J., 1979, *MNRAS*, **187**, 73

Shimizu T. T., et al., 2019, *MNRAS*, **490**, 5860

Silk J., Mamon G. A., 2012, *Research in Astronomy and Astrophysics*, **12**, 917

Spence R. A. W., Tadhunter C. N., Rose M., Rodríguez Zaurín J., 2018, *MNRAS*, **478**, 2438

Storch-Bergmann T., Lopes R. D. S., McGregor P. J., Riffel R. A., Beck T., Martini P., 2010, *MNRAS*, **402**, 819

Storch-Bergmann T., et al., 2018, *ApJ*, **868**, 14

Sun A.-L., Greene J. E., Zakamska N. L., 2017, *ApJ*, **835**, 222

Tadhunter C., et al., 2018, *MNRAS*, **478**, 1558

Tody D., 1986, The IRAF Data Reduction and Analysis System. p. 733, doi:10.1117/12.968154

Treister E., Schawinski K., Urry C. M., Simmons B. D., 2012, *ApJ*, **758**, L39

Trindade Falcão A., et al., 2020, *MNRAS*,

Trump J. R., et al., 2015, *ApJ*, **811**, 26

Unger S. W., Pedlar A., Axon D. J., Whittle M., Meurs E. J. A., Ward M. J., 1987, *MNRAS*, **228**, 671

Villar Martín M., Emonts B., Humphrey A., Cabrera Lavers A., Binette L., 2014, *MNRAS*, **440**, 3202

Villar-Martín M., Arribas S., Emonts B., Humphrey A., Tadhunter C., Bessiere P., Cabrera Lavers A., Ramos Almeida C., 2016, *MNRAS*, **460**, 130

Villar-Martín M., Emonts B., Cabrera Lavers A., Bellocchi E., Alonso Herrero A., Humphrey A., Dall’Agnol de Oliveira B., Storch-Bergmann T., 2021, arXiv e-prints, p. arXiv:2103.06805

Virtanen P., et al., 2020, *Nature Methods*, **17**, 261

Wright E. L., 2006, *PASP*, **118**, 1711

Zubovas K., 2018, *MNRAS*, **479**, 3189

APPENDIX A:

This paper has been typeset from a \LaTeX file prepared by the author.

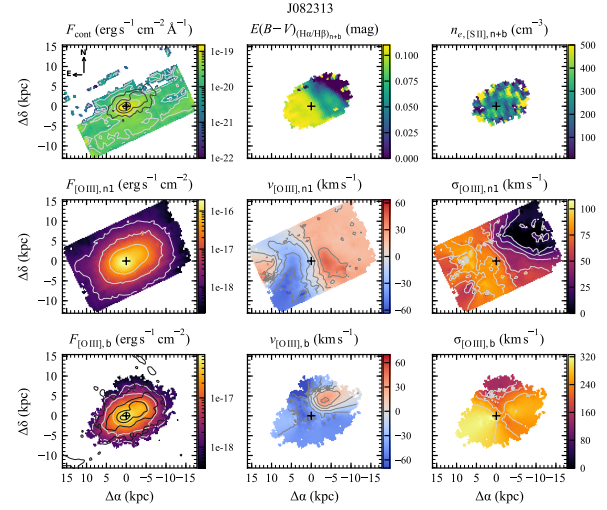


Figure A1. Maps of J082313, similar to Fig. 6. The systemic velocity were calculated from $v_{[\text{O III}],n1}$ (see Section 4.4). Only pixels with $S/N > 3$ are shown. Note that the colorbars have different ranges.

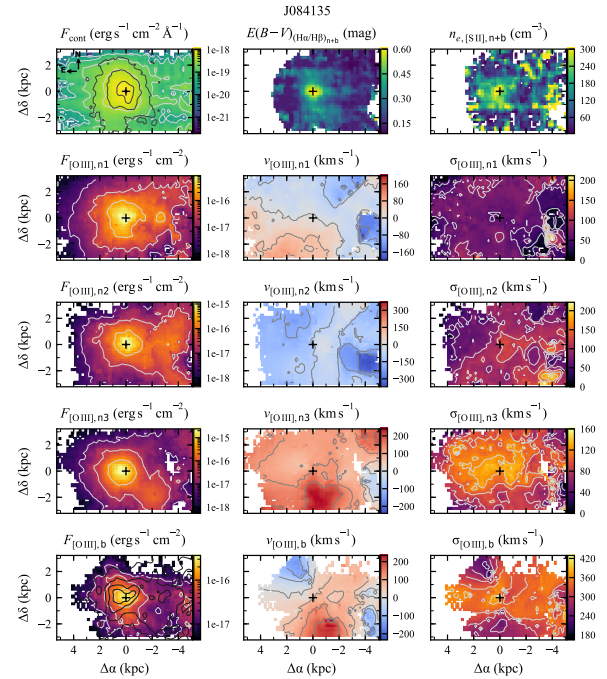


Figure A2. Same as Fig. A1, but for J084135. Systemic velocity calculated from $v_{[\text{O III}],n1}$.

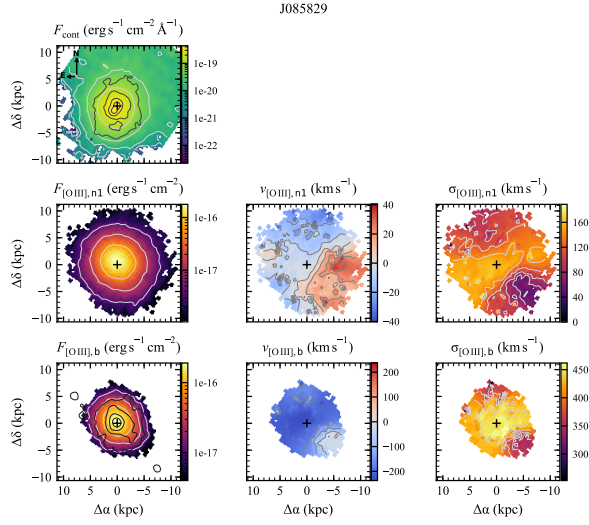


Figure A3. Same as Fig. A1, but for J085829. Systemic velocity calculated from $v_{[\text{O III}]\lambda 4960}$.

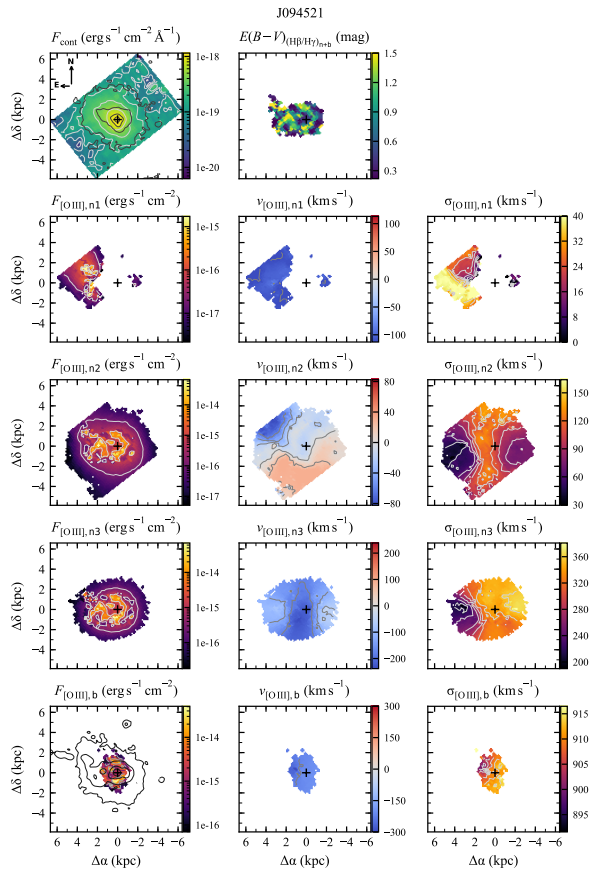


Figure A4. Same as Fig. A1, but for J094521. Systemic velocity calculated from $v_{[\text{O III}]\lambda 5007}$.

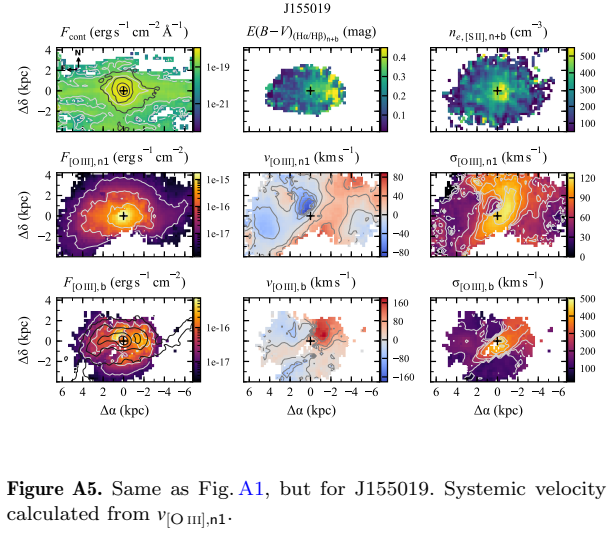


Figure A5. Same as Fig. A1, but for J155019. Systemic velocity calculated from $v_{[\text{O III}]\lambda 4960}$.

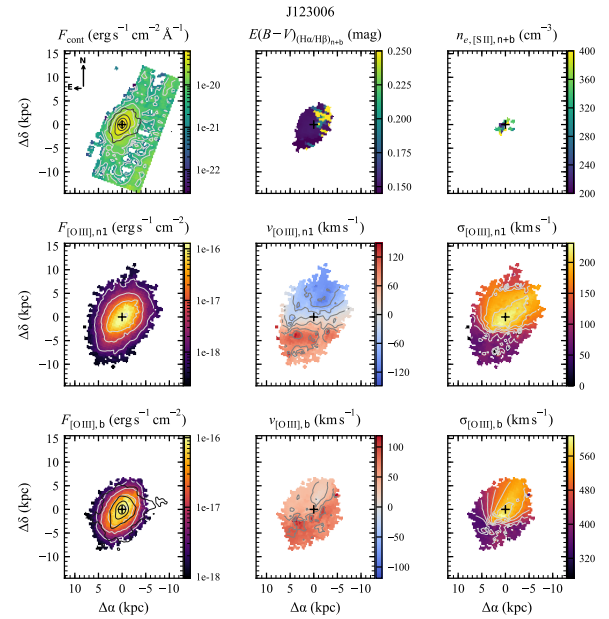


Figure A6. Same as Fig. A1, but for J123006. Systemic velocity calculated from $v_{[\text{O III}]\lambda 4960}$.

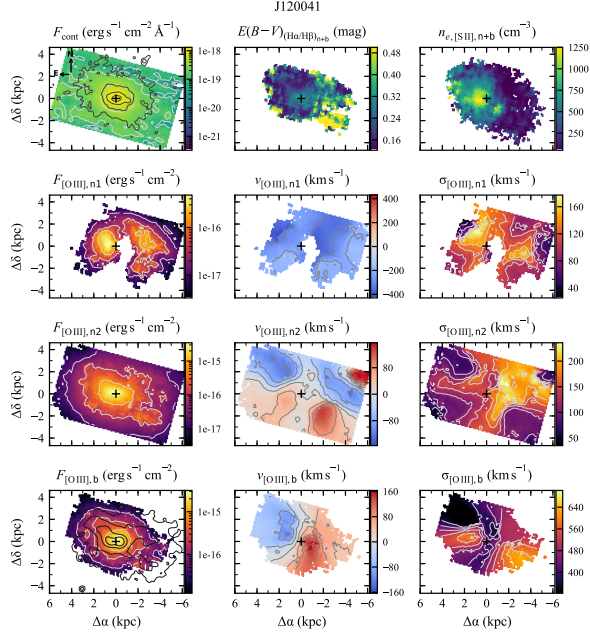


Figure A7. Same as Fig. A1, but for J120041. Systemic velocity calculated from $v_{[\text{O III}], n2}$.

Gauging the effect of Supermassive Black Holes feedback on Quasar host galaxies: Supplementary Appendix

14 April 2021

APPENDIX B:

B1 Telluric absorption correction

Before merging the individual data cubes of each object, we corrected the spectra for telluric absorption using the MOLECFIT software (Smette et al. 2015; Kausch et al. 2015). Besides removing the absorption effect under some emission lines, we retrieved the spectral resolution (σ_{MST} , presented in velocity units in Table 2 in paper) from the model, used later to correct the Gaussian profiles for the instrumental spectral broadening. For each galaxy, we modeled the telluric contribution (O₂ and H₂O bands) in its corresponding standard star, and applied the solution to the science data cubes (see Fig B1). We performed the fit in the stellar spectrum because of its higher signal-to-noise. However, since the observations of the galaxy and the standard star can be months apart, the atmospheric conditions are not the equal. Therefore, before correcting it from the galaxy spectra, we scaled the telluric transmission by a multiplicative factor, minimizing the residuals near an absorption feature.

B2 Broad Line Region (BLR)

Even though our sample consists of QSOs classified as type II (Reyes et al. 2008), one of them – J082313 – showed signs of a weak BLR contribution (only visible in the H α profile).

To model it, we fitted the spectra – obtained from a PSF-size aperture – modeling it with one broad and one narrow components for the NLR gas, along with a broader Gaussian representing the BLR. The other emission lines were also fitted, which helped the NLR model, since we fixed the kinematics of the components between different lines. Fig. B2 (below) shows the resulting fit without (left) and with (right) the BLR component, where $v_{\text{BLR}} = -140 \text{ km s}^{-1}$ and $\sigma_{\text{BLR}} = 1560 \text{ km s}^{-1}$.

With the the BLR component modelled, we repeated the fitting process, now, for all spectra of the data cube. However, in order to account for the smearing effect of the atmospheric seeing, we fixed v_{BLR} and σ_{BLR} at the above values, with the amplitude being the only free parameter of the BLR component. Fig. B2 (top) shows the resulting BLR flux distribution, along with white contours from the 2D-Gaussian best fit model. The resulting FWHM of ~ 0.68 arcsec is in agreement with the seeing obtained from the field in the acquisition image (Table 2 in the paper).

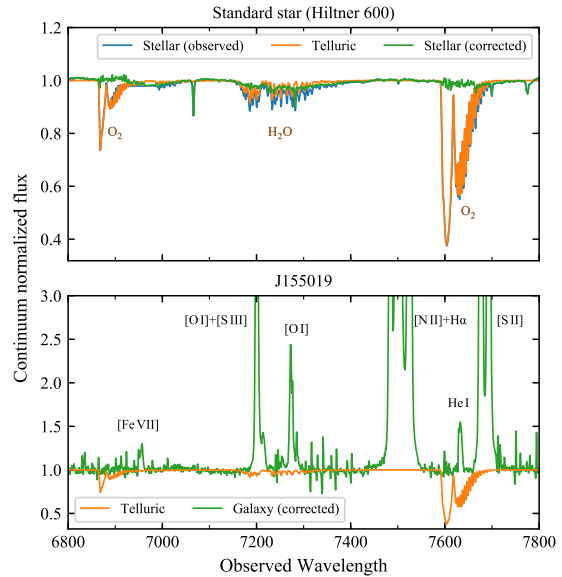


Figure B1. Telluric absorption correction for J155019. The top panel displays the telluric fit (orange) made to the observed standard star continuum-normalized flux (blue), and the result of the correction (green). The bottom axis shows a 2 kpc aperture over the final galaxy data cube (green), after the individual observation were merged and the flux were normalize by the continuum. The telluric transmission (orange) shows how much were corrected it from the O₂ and H₂O absorptions bands.

B3 Source of ionization

In order to identify the main source of ionization in our objects, we generated a BPT diagram (Baldwin et al. 1981) using the total flux ($n+b$) of each emission line (Fig. B3). In this diagram, emission lines with ratios in the region to the left of the dashed and dotted lines (Stasińska et al. 2006; Kewley et al. 2001) can be produced by the radiation originated in star-forming regions in the galaxy. At the right, the solid line (Kewley et al. 2006) separates emission line ratios originated from high-ionization sources (AGNs, above) and low-ionization nuclear emission-line regions (LINERs, below). The parametrizations of the lines were taken from Cid Fernandes et al. (2010). Since the GMOS-IFU spectra of J085829 and J094521 doesn't cover [N II]+H α , we measured [N II] λ 6584/H α in the SDSS spectrum. The diagram

arXiv:2104.06223v1 [astro-ph.GA] 13 Apr 2021

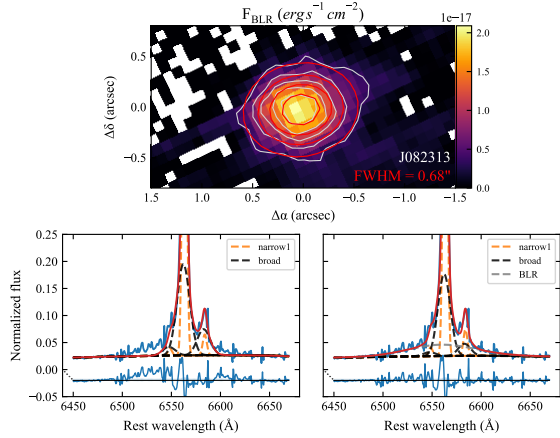


Figure B2. Flux distribution (top) of the J082313 Broad Line Region (BLR) from $H\alpha$, along with its 2D Gaussian fit (white contours). In the bottom, we show the seeing-size aperture spectrum, fitted without (left) and (with) a BLR component (gray). Although the BLR intensity is weak, compared to the NLR components, its addition avoided a wrongly inclusion of another NLR component, which would change the results of our analysis.

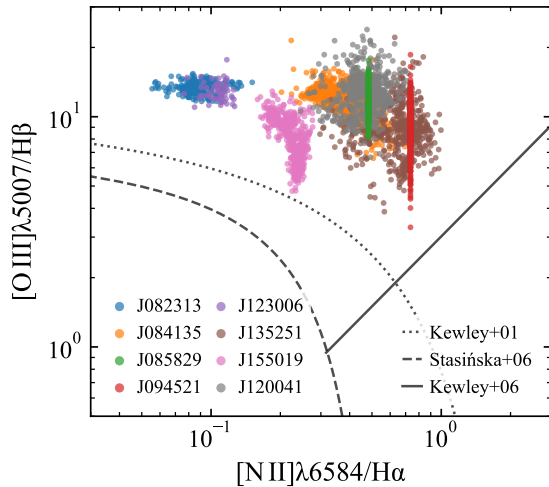


Figure B3. BPT diagram for the galaxies of our sample. The dashed, dotted and solid lines are from Stasińska et al. (2006), Kewley et al. (2001) and (Kewley et al. 2006).

confirms that the observed emission lines of our sample are mostly ionized by AGN sources.

B4 [Ar iv] fit

We applied a Montecarlo method – fitting single Gaussians for each $[\text{Ar IV}]\lambda 4711,40$ emission line (and the near line of $\text{He II}\lambda 4686$) – for the seeing-size apertures spectra of J082313 and J084135 (Fig. B4). We ran 100 iterations, generating new spectra with gaussian noise (standard deviation from the original spectra), and fitting the results, where the $[\text{Ar IV}]$ kinematics were kept equal. From the fits, we obtained the mean and standard deviation values of the

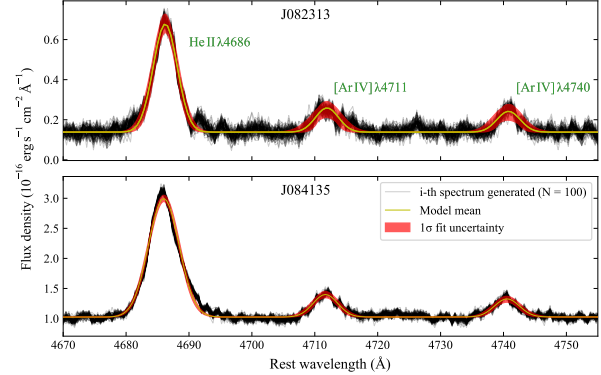


Figure B4. Result of the Montecarlo method, used to fit the $[\text{Ar IV}]\lambda 4711,40$ and $\text{He II}\lambda 4686$ emission lines of J082313 and J08413. We fitted the spectra generated in each run (black lines), with model corresponding to the mean of the parameters shown in yellow. In the red filled region, we display the limits of 100 models, generated using the mean and standard deviation values of the parameters previously fitted.

parameters of the lines, which uncertainties were propagated to the flux ratio of the $[\text{Ar IV}]$ lines, used to obtain $n_{e,[\text{Ar IV}]}$.

B5 Emission line fitting results

An alternative and larger version of Fig. 3 from the paper is shown in Fig. B5.

In Figs. B6–B13, we present results of the fitting process for each QSO of our sample. Different rows correspond to line profiles from different spaxels over the FoV, with the columns displaying a zoom-in on the emission line profiles of $H\beta$, $[\text{O III}]$, $[\text{N II}]$, $H\alpha$ and $[\text{S II}]$.

B6 Maps

In Figs. B14–B21, we present larger versions for the maps of the fitted parameters.

REFERENCES

- Baldwin J. A., Phillips M. M., Terlevich R., 1981, *PASP*, **93**, 5
 Cid Fernandes R., Stasińska G., Schlickmann M. S., Mateus A., Vale Asari N., Schoenell W., Sodr e L., 2010, *MNRAS*, **403**, 1036
 Kausch W., et al., 2015, *A&A*, **576**, A78
 Kewley L. J., Dopita M. A., Sutherland R. S., Heisler C. A., Trevena J., 2001, *ApJ*, **556**, 121
 Kewley L. J., Groves B., Kauffmann G., Heckman T., 2006, *MNRAS*, **372**, 961
 Reyes R., et al., 2008, *AJ*, **136**, 2373
 Smette A., et al., 2015, *A&A*, **576**, A77
 Stasińska G., Cid Fernandes R., Mateus A., Sodr e L., Asari N. V., 2006, *MNRAS*, **371**, 972

This paper has been typeset from a $\text{T}_{\text{E}}\text{X}/\text{L}^{\text{A}}\text{T}_{\text{E}}\text{X}$ file prepared by the author.

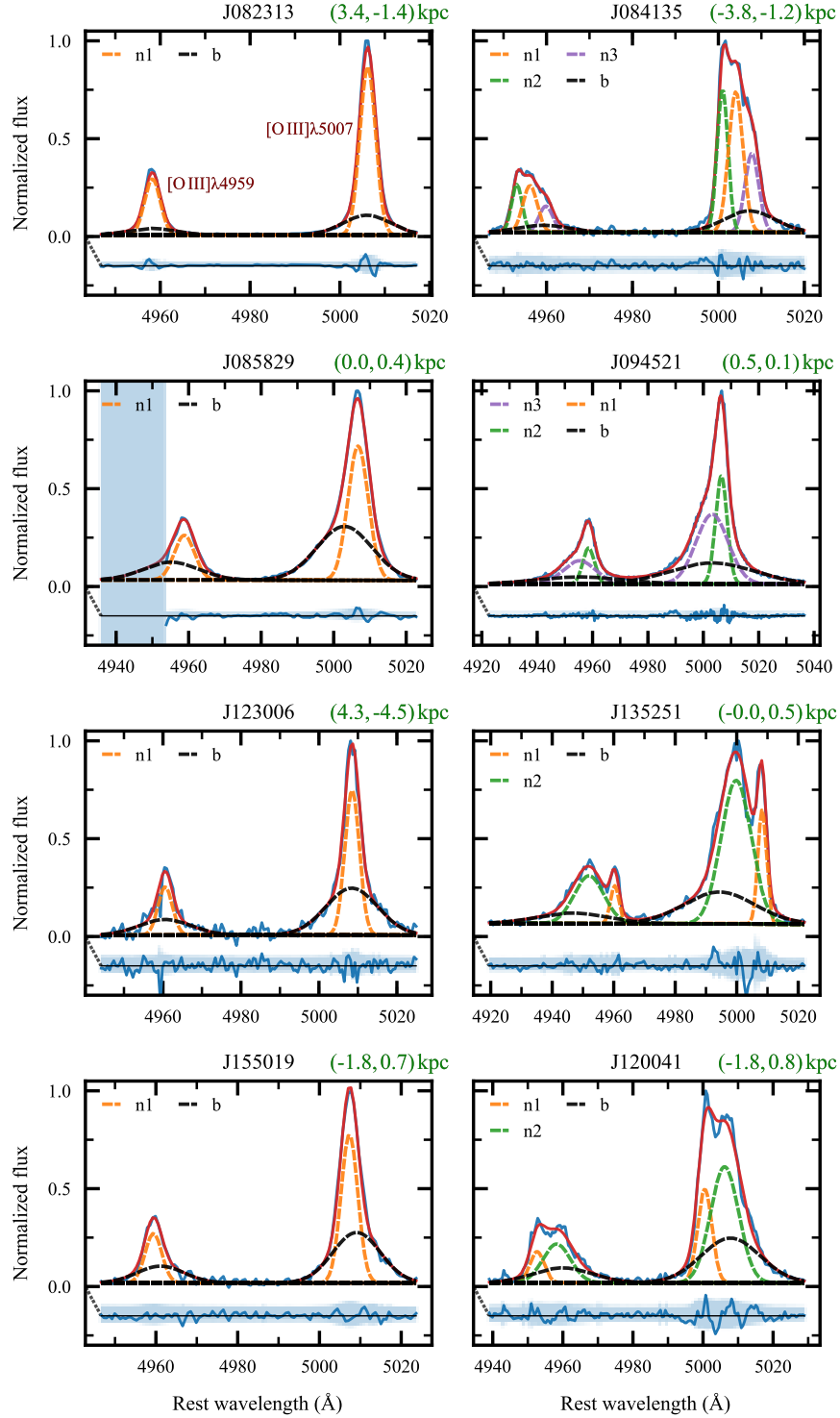


Figure B5. Examples of fitting results for the [O III] line profiles for each galaxy of the sample, highlighting the decomposition of the spectral flux density in narrow (n1, n2, n3) and broad (b) components. The pixel location (projected distance from the nucleus, in kpc) is shown in top right of each panel. Four objects have more than one narrow component, as it can clearly in both [O III] profiles. Here, J094521 does not show its n1 component, that appears in another region of the galaxy, away from the nucleus (see Fig. B9 and Fig. B17)

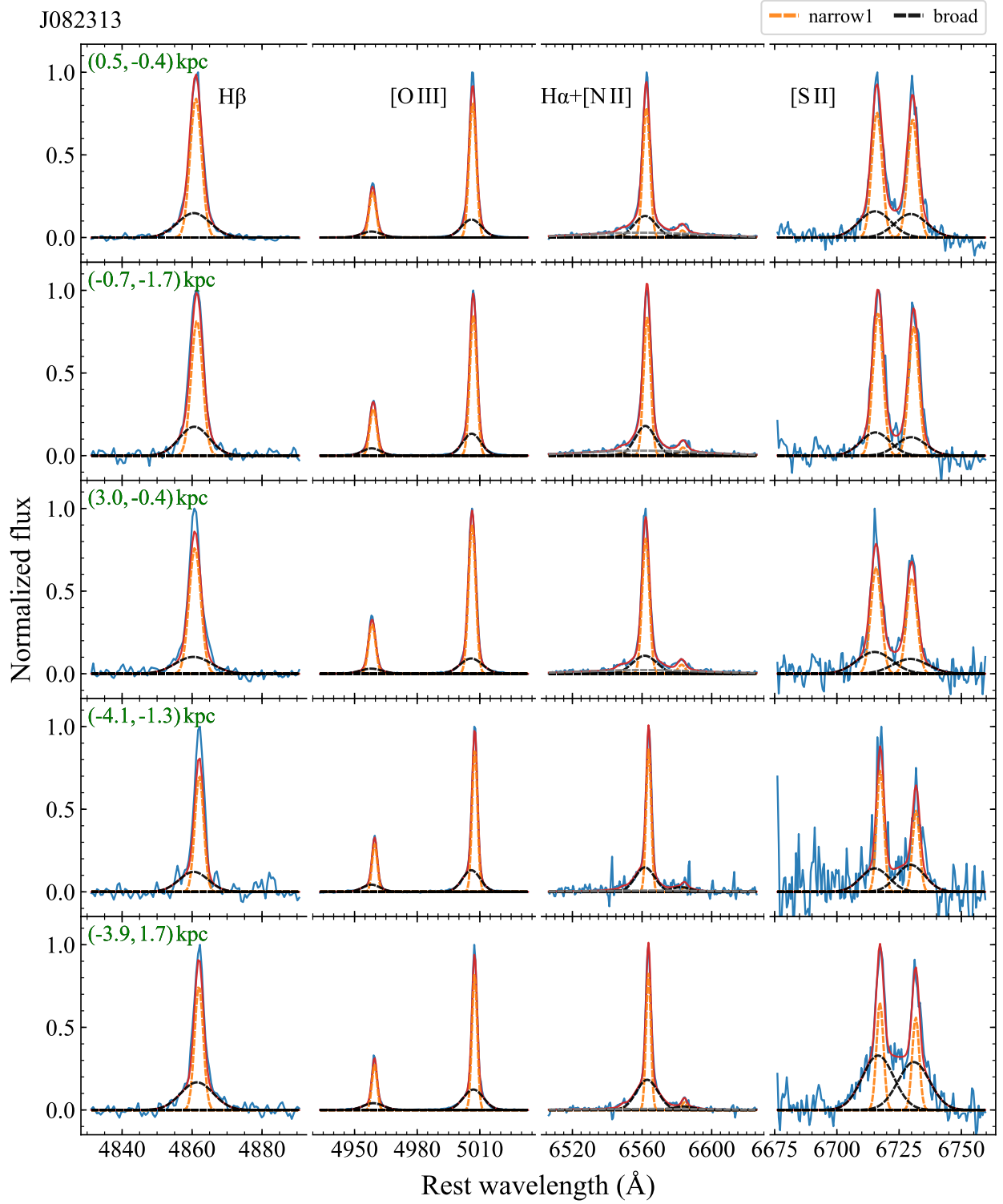


Figure B6. Fitting results for a few spectra of J082313. Each row of the figure corresponds to a different position in the galaxy, identified by $(\Delta\alpha, \Delta\delta)$, the distance from the nucleus (in green at the upper left corner of each row). The columns are zoom-in in the emission lines: $H\beta$, $[O III]$, $(H\alpha + [N II])$ and $[S II]$.

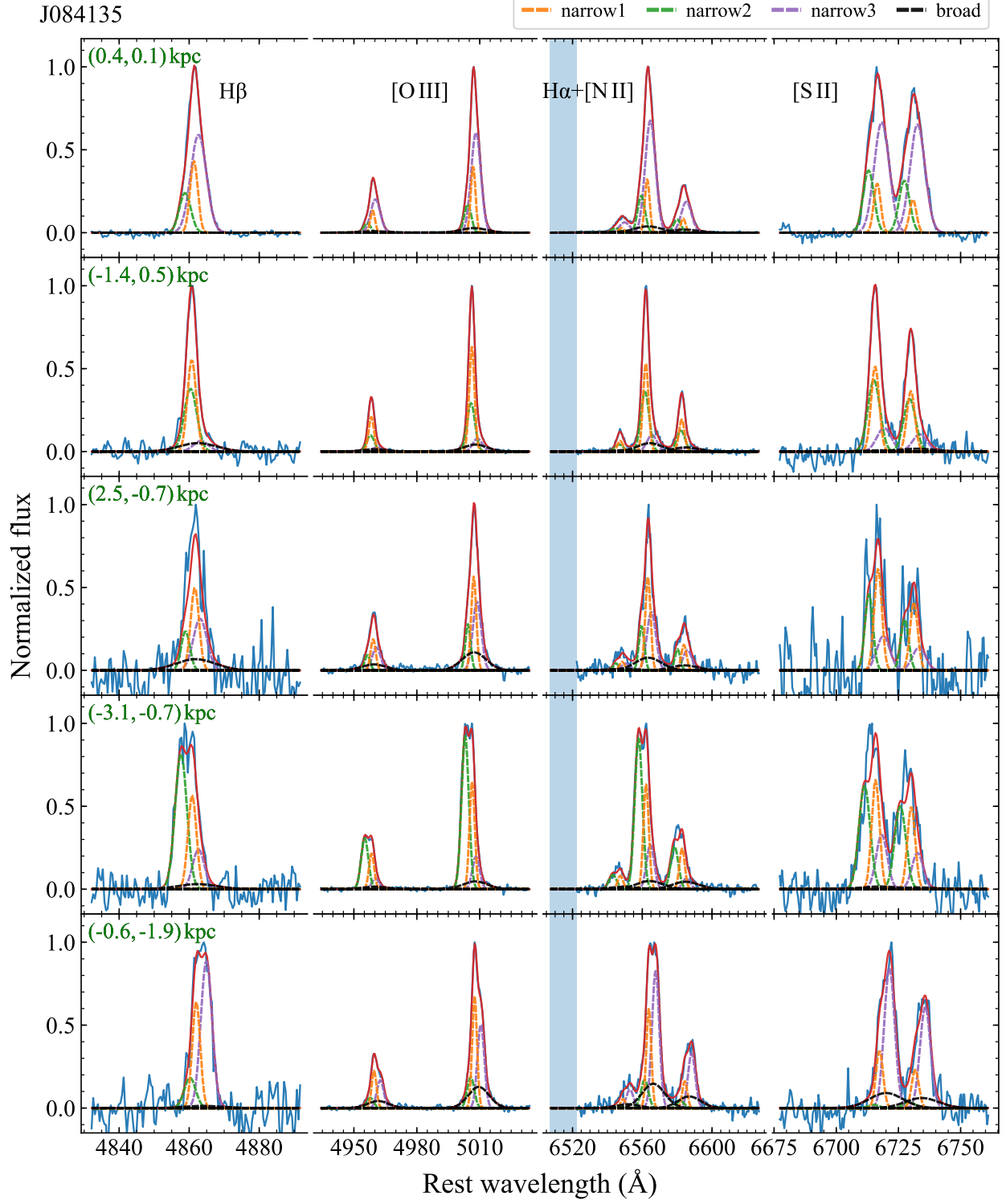


Figure B7. Same as Fig. B6 but for J084135.

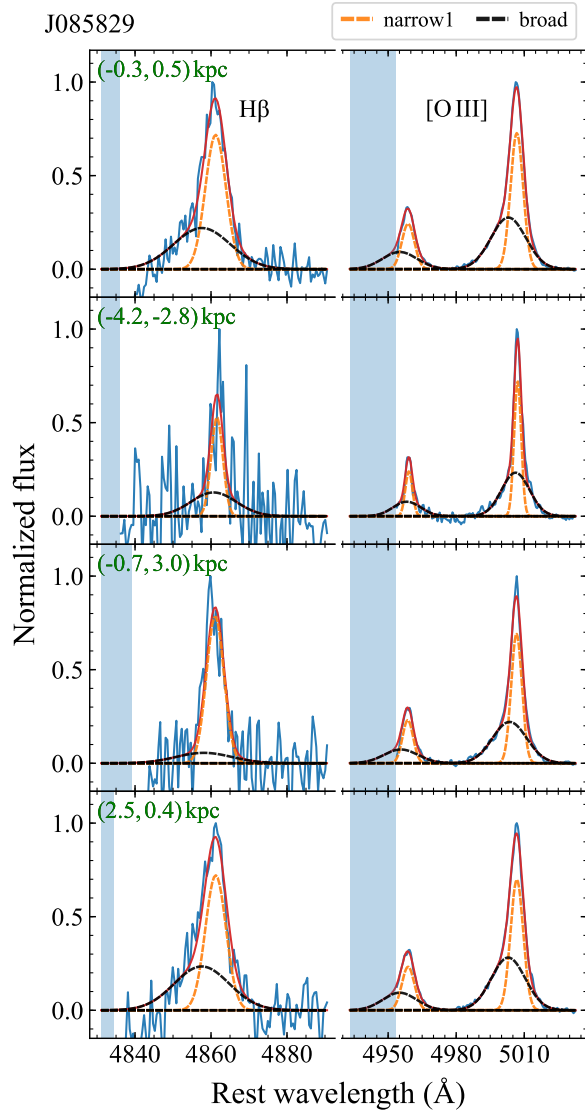


Figure B8. Same as Fig. B6 but for J085829. There were no data in the blue region (due to CCD gaps or bad pixels).

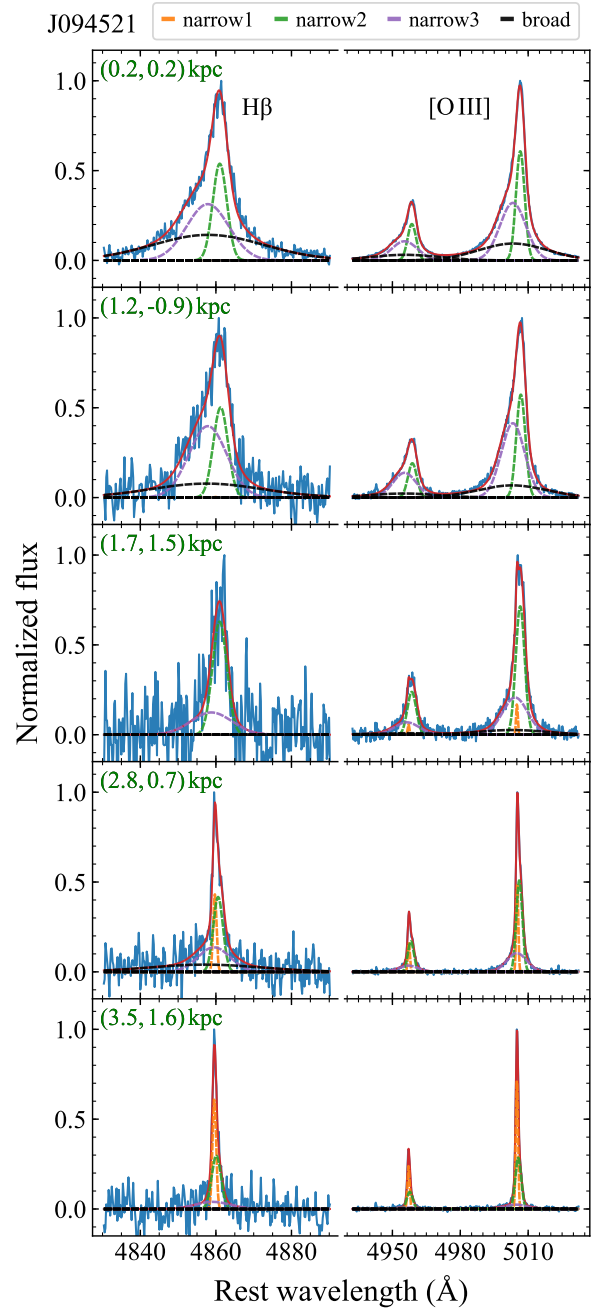


Figure B9. Same as Fig. B6 but for J094521.

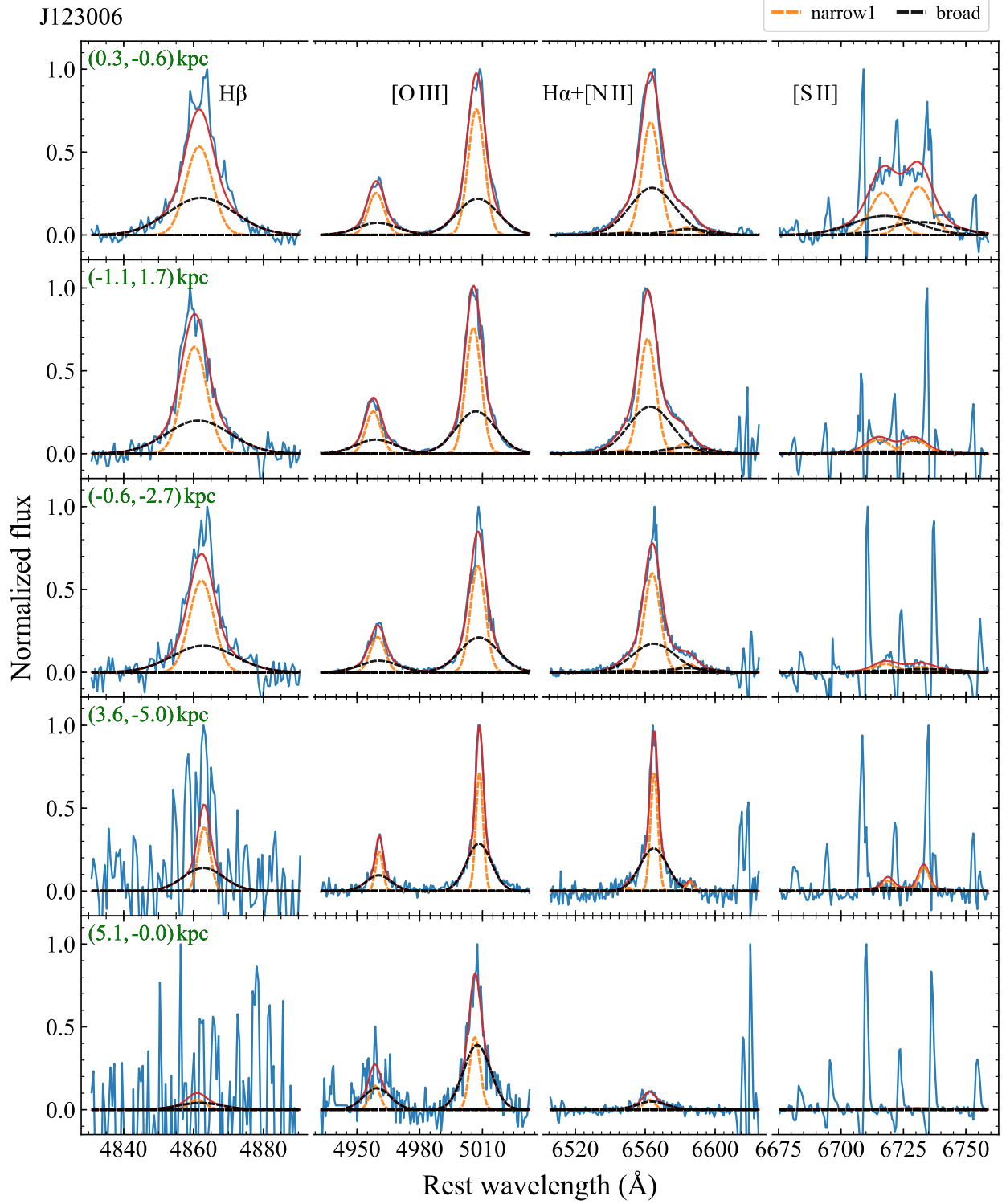


Figure B10. Same as Fig. B6 but for J123006. The telluric emission features were not completely removed from the red part of the spectra, affecting the [S II] measurements. As a consequence, few spaxels had $S/N > 3$ in $F_{[S II]}$, resulting in a low number of $n_{e,n+b}$ data points (see Fig. 6 of the paper).

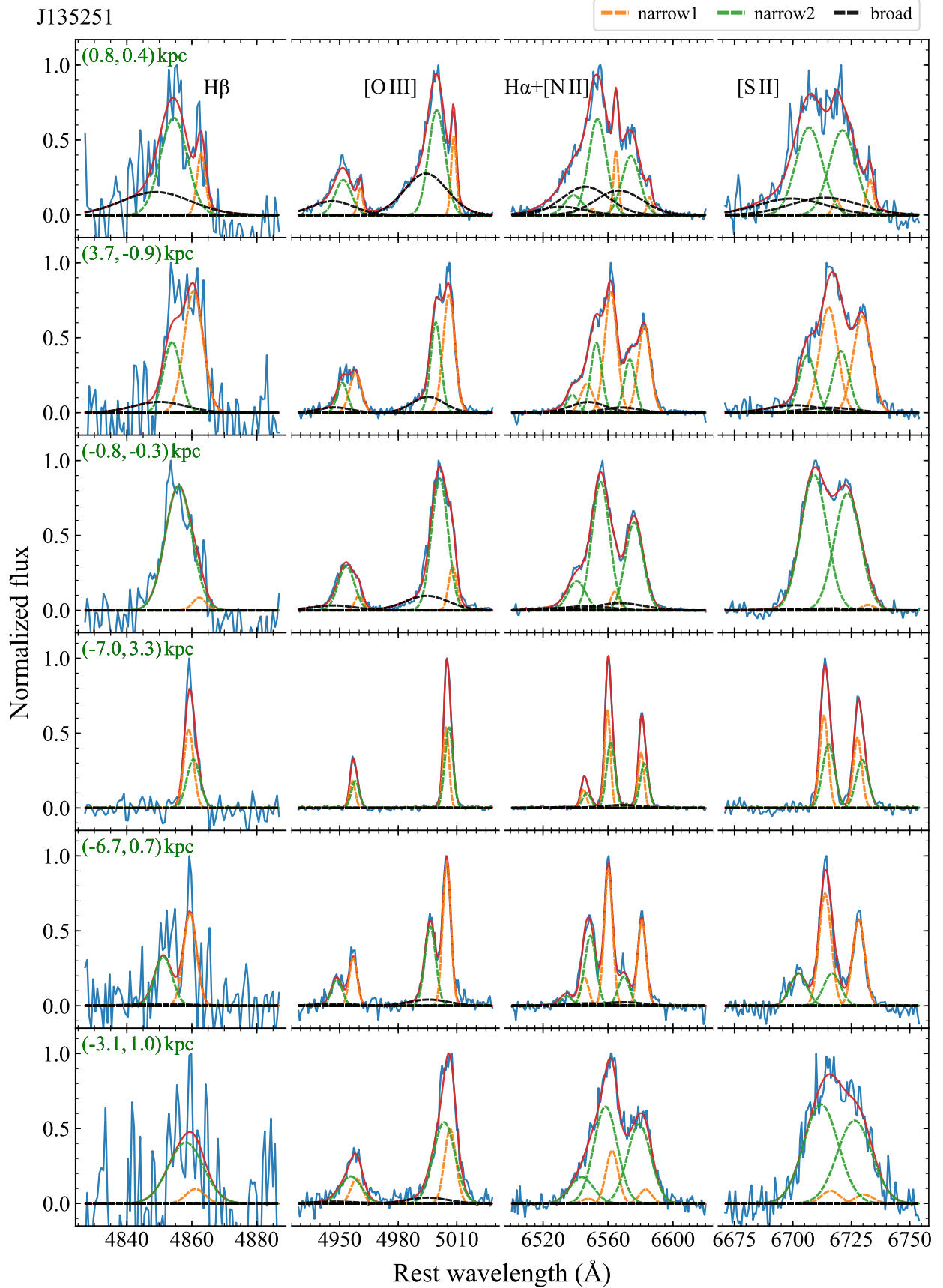


Figure B11. Same as Fig. B6 but for J135251.

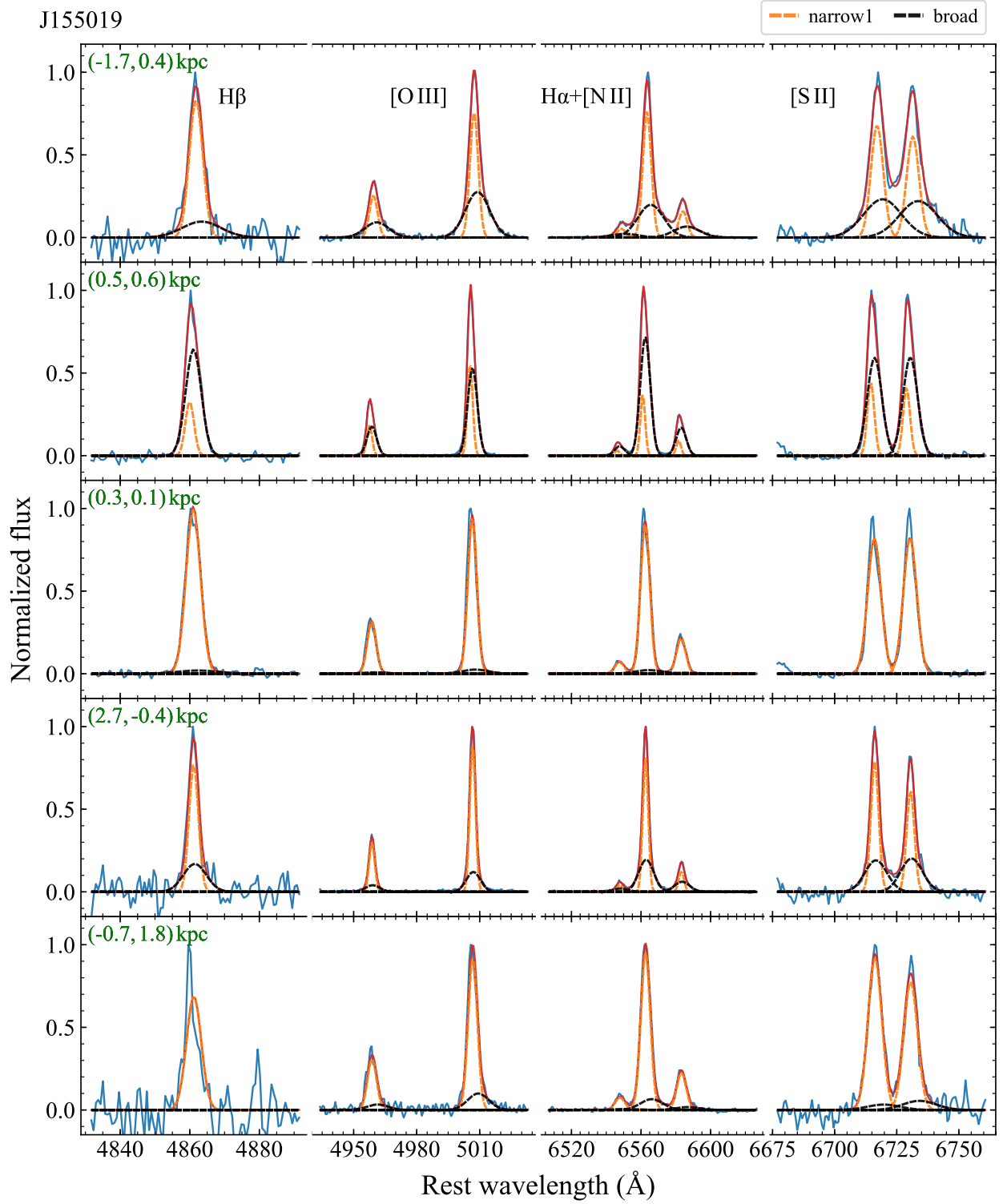
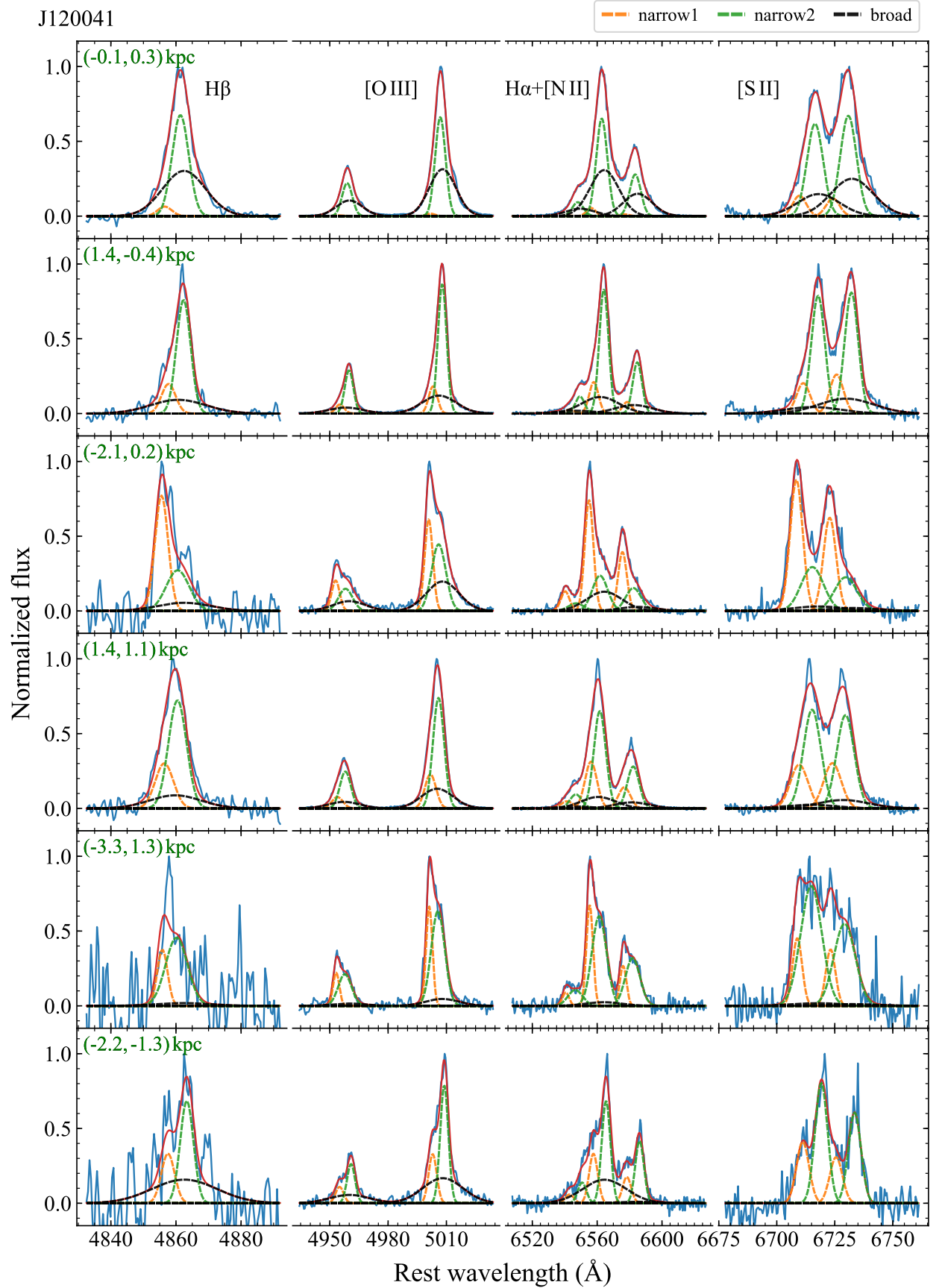


Figure B12. Same as Fig. B6 but for J155019.



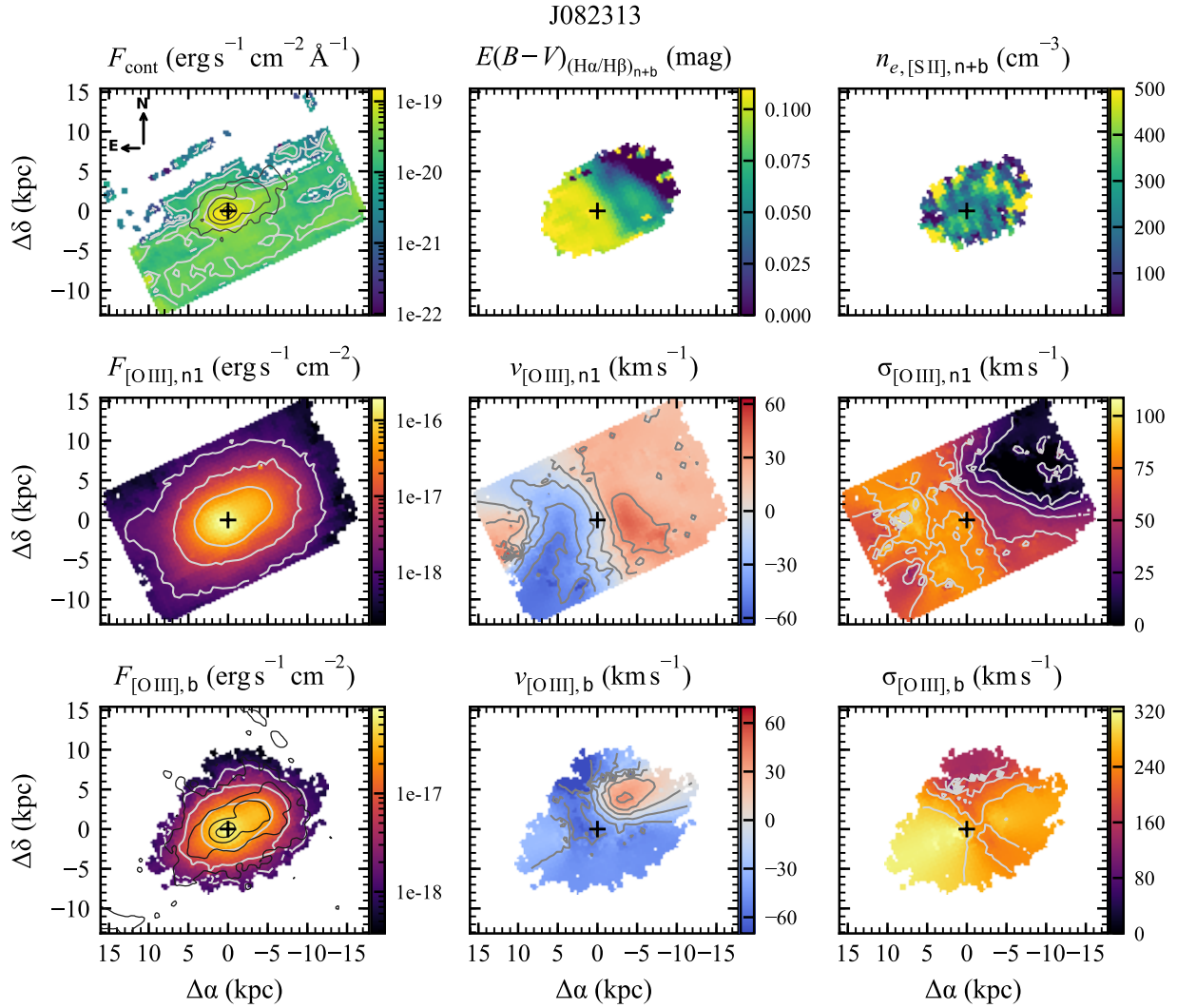


Figure B14. Maps of the measured properties of J08231. In the first row, from left to right, we show: the continuum flux (F_{cont}), the gas reddening ($E(B-V)$), and the electron density (n_e) maps. The remaining rows display maps of the parameters of each $[\text{O III}]\lambda 5007$ component: flux ($F_{[\text{O III}]}$, left); radial velocity ($v_{[\text{O III}]}$, centre); and the velocity dispersion ($\sigma_{[\text{O III}]}$, right column). The last row refers to the broad component, while the remaining middle rows refer to the narrow components ($n1$ and $n2$, in this case). We overplotted the *HST* contours (in black, starting in $3\sigma_{\text{sky}}^{\text{HST}}$) of the continuum (top left) and $[\text{O III}]$ (bottom left) images. North is up and East is left, with the right ascension and declination distances given relative to the continuum peak (black cross). The systemic velocity were calculated from $v_{[\text{O III}],n1}$. Only pixels with $S/N > 3$ are shown. Note that the colorbars have different ranges.

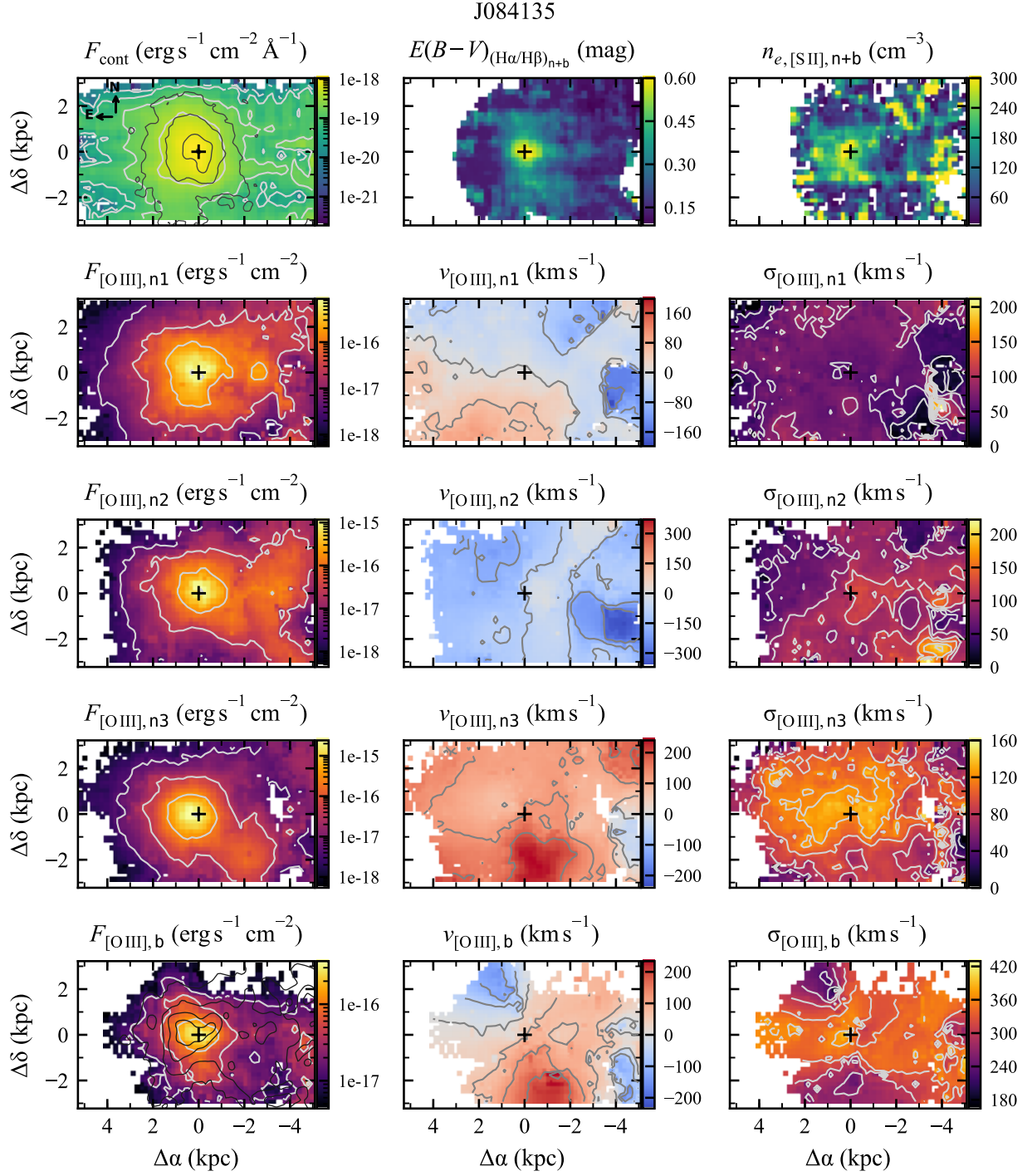
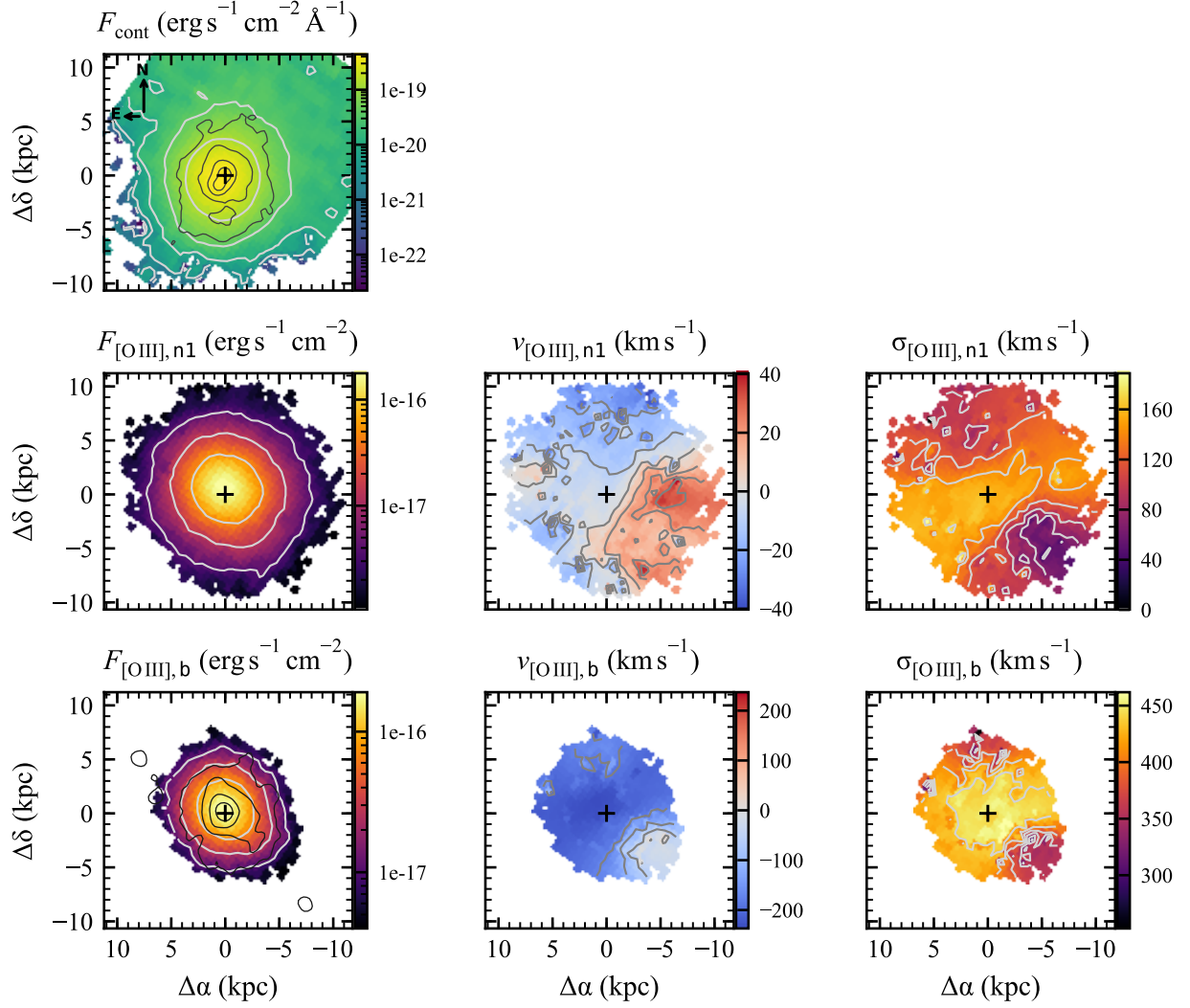


Figure B15. Same as Fig. B14, but for J084135. Systemic velocity calculated from $v_{[\text{O III}], n1}$.

J085829


 Figure B16. Same as Fig. B14, but for J085829. Systemic velocity calculated from $v_{[\text{O III],n1}$.

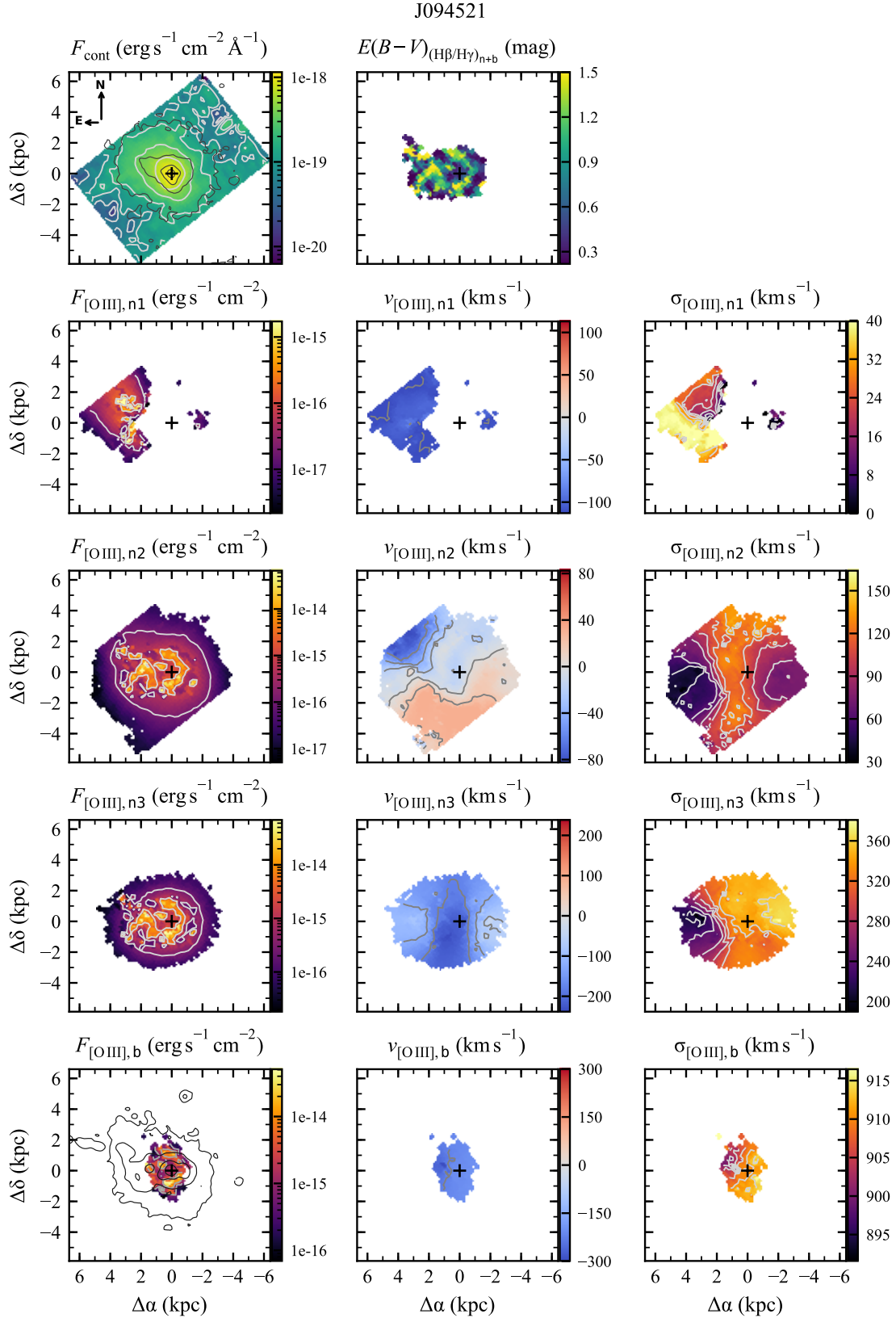


Figure B17. Same as Fig. B14, but for J094521. Systemic velocity calculated from $v_{[\text{O III}]_{n2}}$.

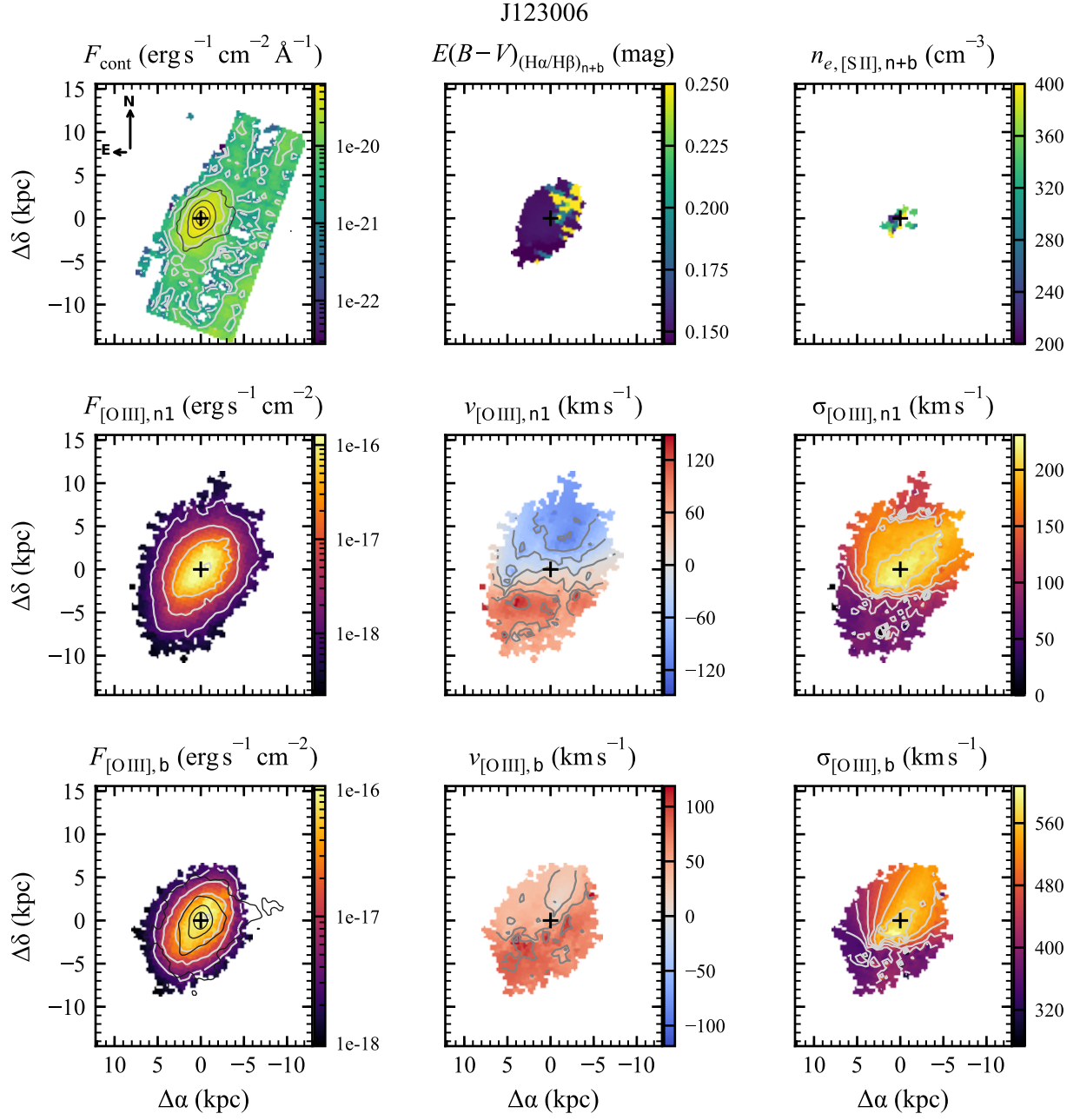


Figure B18. Same as Fig. B14, but for J123006. Systemic velocity calculated from $v_{[\text{O III}], \text{n1}}$.

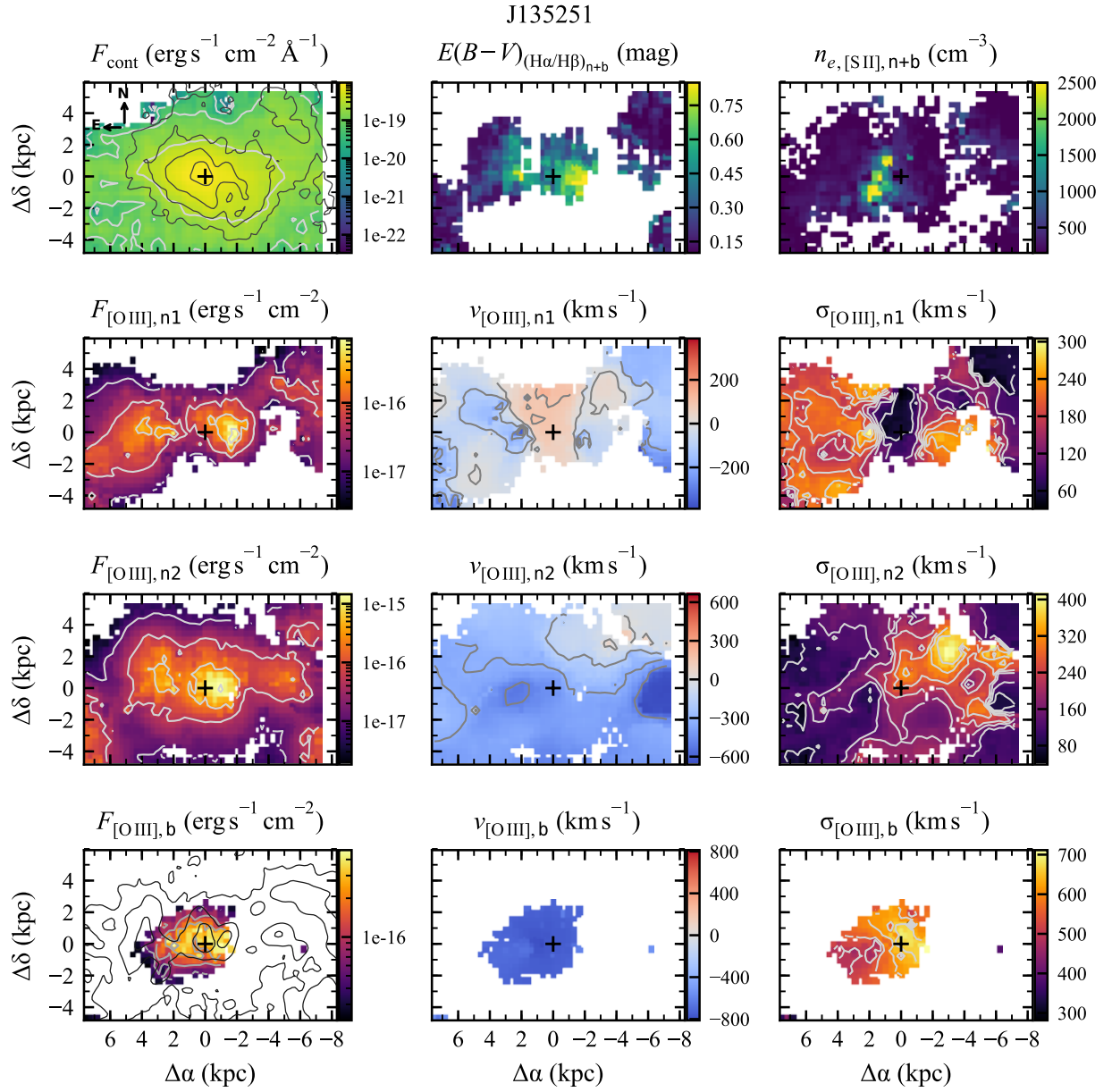


Figure B19. Same as Fig. B14, but for J135251. The systemic velocity were calculated from $v_{[\text{O III}], \text{n1}}$.

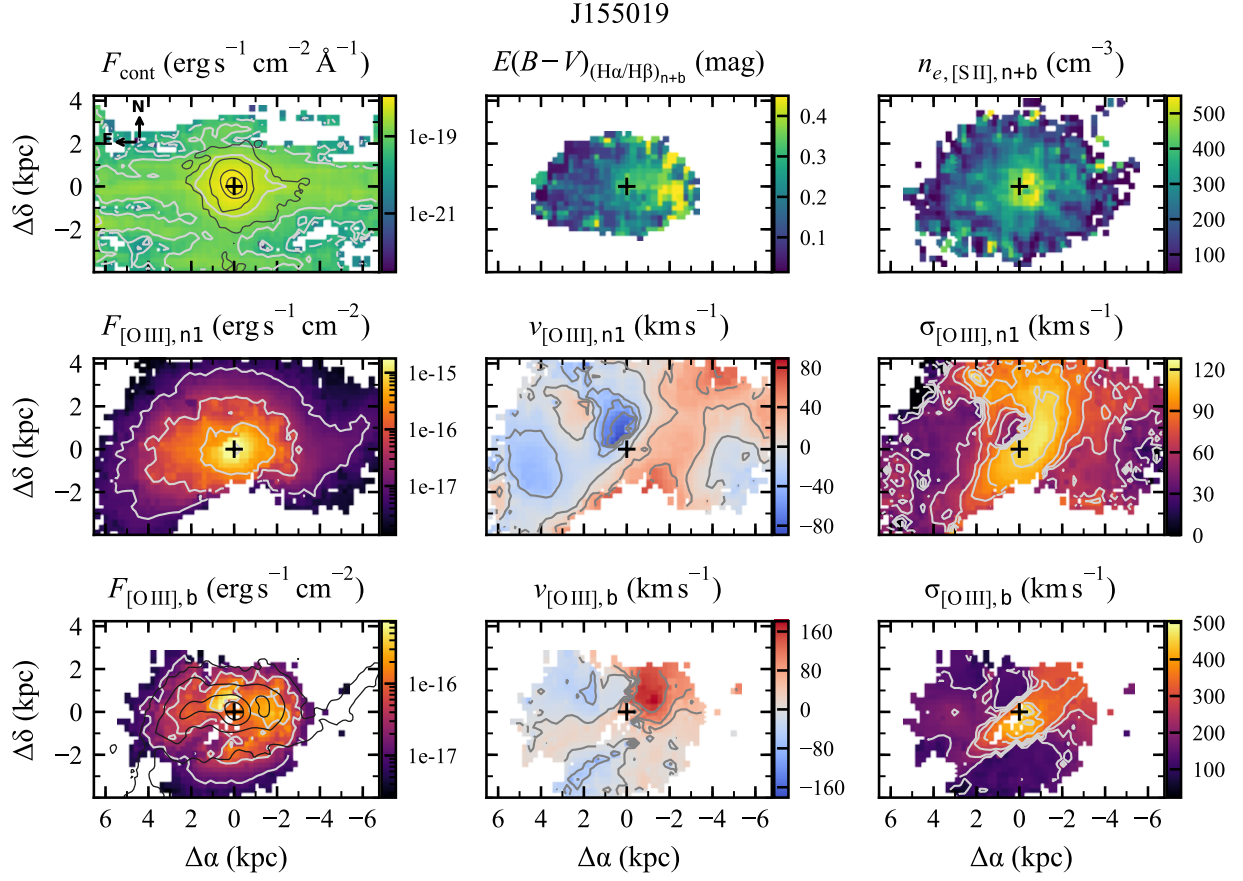


Figure B20. Same as Fig. B14, but for J155019. Systemic velocity calculated from $v_{[\text{O III}]_{\text{n1}}}$.

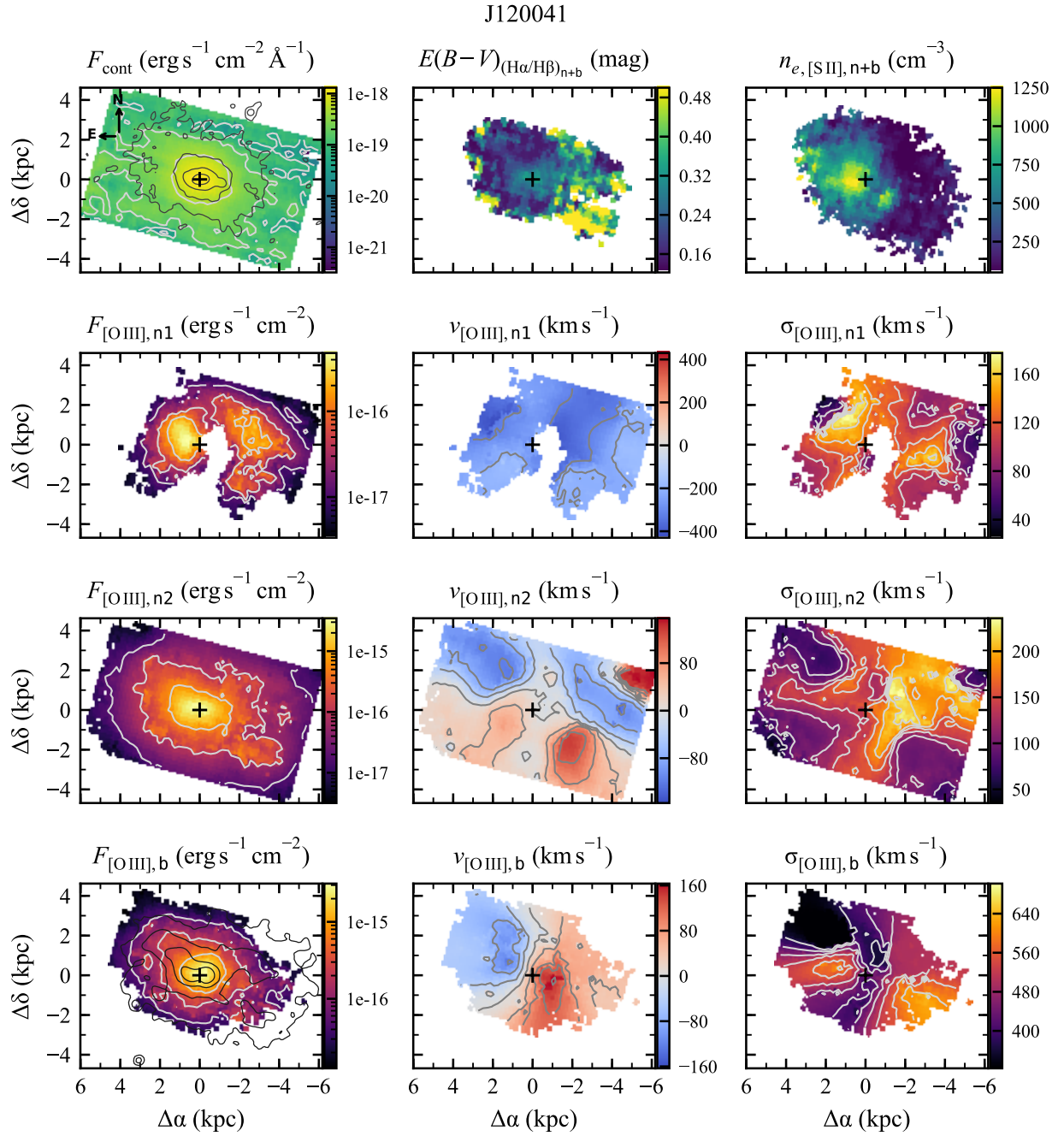


Figure B21. Same as Fig. B14, but for J120041. Systemic velocity calculated from $v_{[\text{O III}], \text{n2}}$.